

1 INTRODUCTION

One of the central challenges in modern astrophysics is to understand how the earliest galaxies and cosmic structures formed from primordial gas just a few hundred million years after the Big Bang (Dayal & Ferrara 2018). The initial fluctuations in the matter power spectrum, determined by the cosmological densities of baryonic and non-baryonic matter, seed the formation of dark matter halos. These halos grow hierarchically by accreting material from the intergalactic medium, ultimately leading to the formation of stars (Press & Schechter 1974; Springel et al. 2005). Beyond the initial efficiency of star formation, stellar feedback plays a key role in regulating ongoing star formation by reducing the gas available for accretion and subsequent star formation (e.g., Agertz & Kravtsov 2015; Gatto et al. 2017). This regulation of star formation influences the number of galaxies of a given luminosity (e.g., Liu et al. 2016; Vogelsberger et al. 2020; Hutter et al. 2021). In addition to the hierarchical evolution of the dark matter halo mass function, baryonic processes—such as star formation efficiency and feedback mechanisms—can also evolve with redshift. In particular, stellar feedback is expected to have the greatest impact on low-mass galaxies, as it is more effective at expelling gas from their shallow gravitational potentials.

The number of galaxies per volume at a given ultraviolet (UV) luminosity, referred to as the UV luminosity function (LF), provides essential insights into the baryonic and non-baryonic processes that govern the growth of early galaxies. In particular, the shape and redshift evolution of the UVLF serve as powerful probes of the efficiency of star formation, the halo mass function, and feedback mechanisms. These processes collectively shape the integrated stellar mass assembly of the Universe. A direct comparison between the redshift evolution of the star formation rate density (SFRD) and the growth of dark matter halos offers critical information on the efficiency of conversion of baryons, namely how effectively gas is converted into stars within halos of varying masses and at different cosmic epochs (Dayal et al. 2014; Mashian et al. 2016).

For over two decades, the *Hubble Space Telescope* (*HST*) has built a remarkable legacy in exploring the high-redshift Universe, discovering thousands of galaxies at redshifts greater than 6 and providing robust constraints on the overall shape of the UVLF during these epochs (Finkelstein et al. 2015; Bouwens et al. 2015; Atek et al. 2018). These results revealed a rapid steepening of the faint-end slope α of the UVLF and a systematic decrease in the number density of bright galaxies from $z = 0$ to $z = 9$, which marks the gradual build-up of the galaxy populations over time. These results were also consistent with the hierarchical growth of dark matter halos and indicated that the star formation efficiency remained relatively constant across cosmic time. However, reaching beyond a redshift of $z \approx 9$, and therefore stepping into the epoch when the first stars formed, had remained challenging due to *HST*'s limited infrared coverage. After two years of operations, the *James Webb Space Telescope* (*JWST*) has identified hundreds of galaxy candidates at redshifts greater than 9, many of which are spectroscopically confirmed and located at record-breaking distances (Finkelstein et al. 2022; Fujimoto et al. 2023; Curtis-Lake et al. 2022; Hainline et al. 2023; Arrabal Haro et al. 2023a; Roberts-Borsani et al. 2023; Bogdan et al. 2023; Carniani et al. 2024).

One of the main challenges arising from the first two years of *JWST* observations is an overabundance of UV-bright galaxies at redshifts beyond $z = 9$ (e.g., Naidu et al. 2022b; Castellano et al. 2023; Finkelstein et al. 2024; Austin et al. 2023; Adams et al. 2024; Chemerynska et al. 2024a) which contrasts with theoretical predictions (e.g., Mason et al. 2015; Crain et al. 2015; Tacchella et al. 2018; Davé et al. 2019;

Yung et al. 2019; Dayal et al. 2019). The evolution of the UV luminosity density, ρ_{UV} , and the corresponding star formation rate density, ρ_{SFR} , is meanwhile significantly slower than anticipated by pre-*JWST* models. This suggests a higher-than-expected production rate of UV photons at redshifts beyond $z = 8$ (Naidu et al. 2022b; Castellano et al. 2023; Chemerynska et al. 2024a). This has now been observed in an increasingly large number of studies and independent fields, reducing potential field-to-field or environment-dependent variations (Donnan et al. 2024; Bouwens et al. 2023; McLeod et al. 2024; Austin et al. 2023; Adams et al. 2024). Several physical scenarios are being explored to explain this slower than expected redshift evolution of the bright-end of the UVLF. These include (i) strong radiation-driven outflows that clear the dust content from star-forming regions in early galaxies (Ferrara 2024); effectively reducing the attenuation and increasing the UV luminosity of galaxies at all masses; (ii) the occurrence of reduced or feedback-free starbursts (FFBs) (Dekel et al. 2023); producing an increase in star formation efficiency above a mass threshold that declines with redshift, leading to an increase in the luminosity of massive galaxies; (iii) a stochastic star formation history (e.g., Ciesla et al. 2024a; Muñoz et al. 2023; Pallottini & Ferrara 2023; Sun et al. 2023; Shen et al. 2023; Endsley et al. 2024) which results in some low-mass galaxies contributing to the bright-end of the UVLF.

However, it remains unclear whether this slower evolution also extends to the faint-end of the UV luminosity function, where star formation efficiencies are expected to differ, or where stellar feedback might efficiently remove gas from the shallow gravitational potentials in these low-mass galaxies. Moreover, the physical motivations for ascribing the various scenarios have differing and testable, implications for the faint-end part of the LF. Surprisingly, this population of faint galaxies has remained largely unexplored in *JWST* programs to date. This is primarily due to the programs' limited depth or their focus on targeting blank fields. Importantly, in standard Λ CDM, lower-mass halos are substantially more abundant than higher-mass halos, potentially implying that the bulk of early star formation might reside in this hitherto unexplored faint-end range of the UVLF.

In this work, we report on the results of our analysis of the lensing-augmented observations of the *JWST* GLIMPSE program (PIs: Atek & Chisholm, JWST-GO-3293). GLIMPSE obtained ultra-deep NIR-Cam observations of the $z = 0.35$ lensing cluster Abell S1063. Here, we present a comprehensive study of the faint-end of the galaxy UVLF and its evolution from $z \sim 9$ to $z \sim 15$. This work builds on a comprehensive characterization of the lensing effects, which permits us to probe the ultra-faint population of galaxies at these early epochs. We also derive the SFRD evolution across this redshift range integrating it for the first time down to the faintest magnitude reached thus far and explore its implications on galaxy formation models. This evolution is crucial for understanding the assembly of mass onto the very first DM halos, which seed large-scale structure formation in the Universe.

The paper is organized as follows: In Section 2, we introduce the GLIMPSE survey and the associated *JWST* observations, providing a detailed description of the data reduction process and photometric measurements. Section 3 focuses on the mass model and the strong lensing constraints of Abell S1063. In Section 4, we outline the methodology used to identify high-redshift galaxy candidates. Our approach to characterizing the effective survey parameters is described in Section 5, which includes completeness estimates (Section 5.1) and the survey volume estimation (Section 5.2). The UV luminosity function results, along with comparisons to previous studies as well as theoretical predictions, are presented in Section 6. The cosmic SFR density and its redshift evolution are discussed in detail

in Section 7. Finally, Section 8 provides a summary of our findings and conclusions of our work.

Throughout this work, we assume a flat Λ CDM cosmology with $H_0 = 70 \text{ km s}^{-1} \text{ Mpc}^{-1}$, $\Omega_M = 0.3$ and $\Omega_\Lambda = 0.7$.

2 THE JWST GLIMPSE PROGRAM

This study utilizes ultra-deep NIRCam imaging of the lensing cluster Abell S1063 ($\alpha = 22^{\text{h}}48^{\text{m}}44.13^{\text{s}}$, $\delta = -44^{\circ}31'57.50''$) at a redshift of $z = 0.348$, obtained through the *JWST* large program GLIMPSE (PIs Atek & Chisholm). The observations include imaging data in seven broadband filters (F090W, F115W, F150W, F200W, F277W, F356W, and F444W) and two medium-band filters (F410M and F480M), achieving an unprecedented depth in the broadbands of approximately 30.8 mag at 5σ over the $0.8 - 5\mu\text{m}$ wavelength range. Data reduction followed the procedure described in [Endsley et al. \(2024\)](#), using the `jwst_1293.pmap` reference file, with further details provided in the GLIMPSE overview paper (Atek in prep.).

The reduction process included various enhancements beyond the standard Space Telescope Science Institute (STScI) pipeline, such as background subtraction, artifact correction, and cosmic ray rejection. To further improve the depth and access the immediate surroundings of the cluster field, we subtracted the bright cluster galaxies (bCGs) and intra-cluster light (ICL) from the images following methods outlined in [Shipley et al. \(2018\)](#); [Weaver et al. \(2024\)](#) and implemented in [Suess et al. \(2024\)](#). Additionally, we incorporated ancillary *HST* observations from the Hubble Frontier Fields (HFF; [Lotz et al. 2017](#)) and BUFFALO programs ([Steinhardt et al. 2020](#)). Prior to photometric measurements, we constructed empirical point spread function (PSF) models from stars in the field, convolving all *JWST* and *HST* images to the broadest PSF model, F480M in this case.

We performed source extraction on an inverse-variance weighted stack of the short-wavelength (SW) filters F090W+F115W+F150W+F200W and the long-wavelength (LW) filters F277W+F356W+F444W using SExtractor ([Bertin & Arnouts 1996](#)). This process enables the SW bands to provide a factor of two improvement in spatial resolution compared to the LW bands. However, it may miss dusty or high-redshift galaxies that are detectable in the LW bands. To address this, we merged the SW and LW detection catalogs, retaining all sources from the SW catalog and including only those LW-detected sources whose central pixel falls within a region of the SW segmentation map with a value of zero, indicating no previously associated source. The photometry was computed within $D = 0.2''$ apertures with PHOTUTILS. Uncertainties on the photometry were calculated using the standard deviation within 2000 random apertures placed in adjacent source-free regions of the images. To minimise the number of spurious objects, we excluded all sources located along diffraction spikes of bright stars, within $0.6''$ of the edge of the image, and within a $2''$ circle around a bCG. To perform the aperture corrections, we used the empirical PSF curves of growth to account for the fraction of the flux that falls outside our aperture size.

3 GRAVITATIONAL LENSING

To accurately constrain the high-redshift UVLF, it is crucial to have a robust gravitational lensing model of the foreground galaxy cluster lens in order to calculate the magnifications of the distant background sources and the survey volume. For GLIMPSE, we utilize a new parametric strong lensing (SL) model of AS1063, constructed

with an updated version of the [Zitrin et al. \(2015\)](#) analytic method (see [Furtak et al. 2023](#)). The model is fully analytic, in the sense that it is not limited to a prefixed grid resolution, which enables faster computation and higher resolution results. We model the cluster with two large-scale smooth dark matter (DM) halos, both parametrized as pseudo-isothermal elliptical mass distributions (PIEMDs; [Kassiola & Kovner 1993](#)). One halo is centered on the brightest cluster galaxy, while the other is positioned near a group of galaxies in the north-eastern region of the cluster (e.g., [Bergamini et al. 2019](#); [Beauchesne et al. 2024](#)), slightly outside the field-of-view of GLIMPSE. Additionally, we model the 303 cluster member galaxies as dual pseudo-isothermal ellipsoids (dPIEs; [Elíasdóttir et al. 2007](#); [Natarajan & Kneib 1997](#)). This relative simplicity of the mass distribution of AS1063 is the reason it was chosen by the GLIMPSE program, as this minimizes the lensing induced systematics typical for more complex SL clusters (e.g., [Acebron et al. 2017](#); [Atek et al. 2018](#); [Limousin et al. 2024](#)). The mass model is constrained with 75 multiple images, detected with *HST* and MUSE, of 28 distinct sources, of which 24 have spectroscopic redshifts ([Balestra et al. 2013](#); [Richard et al. 2021](#); [Beauchesne et al. 2024](#); [Topping et al. 2024a](#)). We also use the parity information of a few arcs to further constrain the model. The model optimized a Monte-Carlo Markov Chain (MCMC) analysis and achieves a final lens-plane image reproduction RMS of $\Delta_{\text{RMS}} = 0.54''$. We refer the reader to Furtak et al. (in prep.) for more details on the mass modeling. A preliminary version of this model was previously also deployed in the analyses presented in [Topping et al. \(2024a\)](#), [Kokorev et al. \(2025\)](#), and [Fujimoto et al. \(2025\)](#).

We obtain magnification factors and their uncertainties for our sample by calculating the deflection at the position and photometric redshift of each object. The magnification uncertainties are drawn from the best-fit model's posterior distribution. In order to further account for typical SL systematics, conservatively, we add a systematic component of 15 % to the magnification uncertainties (e.g., [Zitrin et al. 2015](#)). We use the model to verify if sources in our sample are multiply-imaged in section 4. We also construct the high-redshift source planes used for the volume computations in section 5.1 and calculate the cumulative source plane areas as a function of magnification.

4 HIGH-REDSHIFT GALAXY SAMPLE

We begin by identifying high-redshift galaxy candidates using a color-color dropout selection, which relies on detecting the Lyman break caused by intergalactic medium (IGM) absorption (e.g., [Steidel et al. 1996](#); [Giavalisco 2002](#)). Galaxies in the redshift range $9 < z < 11$ dropout in the F115W filter, and galaxies between $z = 11 - 15$ drop out in the F150W filter. To establish optimal high-redshift selection criteria, we computed color-color tracks for a range of galaxy templates and potential contaminating sources ([Atek et al. 2023a](#)). Using BEAGLE ([Chevallard & Charlot 2016](#)), we generated star-forming galaxy templates at redshifts 8 to 20 with dust attenuation values (Av) ranging between 0 and 0.5 mag, adopting the SMC extinction curve ([Pei 1992](#); [Reddy et al. 2015](#)). To define a color space that minimizes contamination from low- z interlopers, we also included quiescent galaxies simulated with GRASIL ([Silva et al. 1998](#)) from the SWIRE library ([Polletta et al. 2007](#)), with attenuation ranging from $\text{Av} = 1$ to 3 mags. Additionally, we incorporated brown dwarf interloper templates from [Chabrier et al. \(2000\)](#) and [Allard et al. \(2001\)](#). Finally, we computed synthetic photometry across all *JWST* bands and established Lyman break criteria for each dropout (redshift) sample.

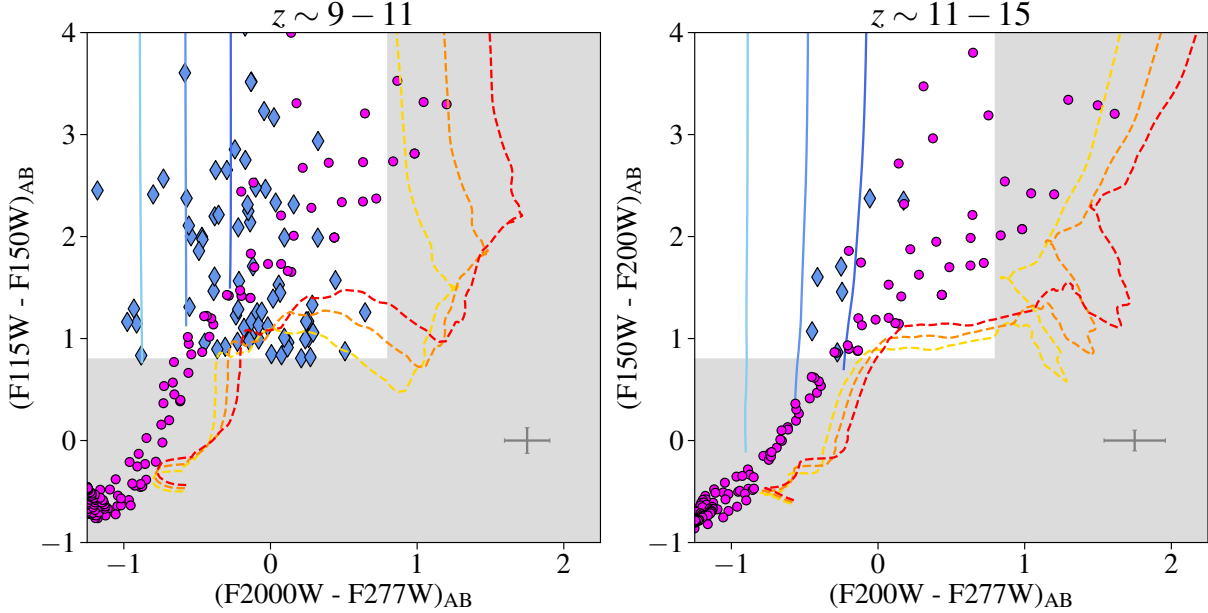


Figure 1. Color-color diagram for the high-redshift galaxy selection at $z \sim 9 - 11$ and $11 - 15$ (from left to right). The selected candidates are shown in blue diamonds with the selection window (white area) defined by the equations (1) and (2), respectively. The grey cross on the lower-right of each panel represents the average $1 - \sigma$ uncertainty on the measured colors. The blue-solid lines are the expected color-color tracks of typical starburst galaxies at $z > 9$ based on galaxy templates generated by BEAGLE (see Sect. 4 for details). The colored-dashed lines are color tracks of quiescent galaxies (potential low-redshift contaminants). Different values of attenuation were applied for high- z starburst and low- z quiescent templates, $A_v = [0, 0.25, 0.5]$ (yellow to red; blue to dark blue), assuming the SMC dust law. The magenta points show the color evolution of cold stars: brown dwarfs and M-class (Chabrier et al. 2000; Allard et al. 2001).

Galaxies in the redshift range $9 < z < 11$ must satisfy the following color-color criteria:

$$\begin{aligned} m_{115} - m_{150} &> 0.8 \\ \wedge m_{150} - m_{200} &< 0.8 \vee m_{200} - m_{277} < 0.8 \end{aligned} \quad (1)$$

and for $11 < z < 15$ galaxies, we adopt the following criteria:

$$\begin{aligned} m_{150} - m_{200} &> 0.8 \\ \wedge m_{200} - m_{277} &< 0.8 \vee m_{277} - m_{356} < 0.8 \end{aligned} \quad (2)$$

where the first criterion picks the dropouts, while the other two criteria are used to exclude red contaminants. For each redshift range, we apply the following additional criteria to ensure the robustness of our sample. First, sources must be detected at the level higher than 3σ in bands red-ward of the break and at the 5σ level in at least one band. We also exclude any source detected above the 2σ level in any band blue-ward of the break. When calculating the Lyman break, if a source's detection level falls below the 1σ magnitude limit in the dropout band, we substitute its magnitude with the 1σ uncertainty from the aperture measurement. Additionally, all sources undergo visual inspection to remove any remaining artifacts or spurious detections, such as residual diffraction spikes that were not flagged or contamination by a bright neighbouring object. To minimize contamination by dwarf stars, we also verify that our candidates are not point-source like and are not too compact. Figure 1 illustrates the process of dropout selection and the color-color window adopted for each redshift range. The galaxy candidates are shown in the color-color diagram alongside the main sources of contamination.

In parallel, we computed photometric redshifts for the entire catalog of sources using the Python implementation of EAZY (Brammer et al. 2008). The analysis incorporated the *JWST* GLIMPSE photometry, utilizing aperture-corrected $D = 0.2''$ *JWST* flux densities. We adopted the `blue_sfhz_13` template library, which includes redshift-dependent star formation histories based on high- z results

from recent *JWST* observations (Carnall et al. 2023), as well as dust attenuation (Calzetti et al. 2000) and IGM attenuation (Asada et al. 2024). The redshift grid spanned the full range, from $z = 0.01$ to $z = 30$. In the end, all the dropout-selected sources have best-fit photometric redshifts within the selection window. Hereafter, we adopt the EAZY best-fit solution as the photometric redshift, along with the corresponding uncertainty derived from the redshift probability distribution. The final galaxy sample contains 98 galaxies at $z \sim 9 - 11$ and 7 galaxies at $z \sim 11 - 15$. The positions of the galaxy candidates in the GLIMPSE field are illustrated in Figure 2 and the full list of the sample is provided in Table A1. Figure 3 presents the intrinsic (de-lensed) UV magnitude of the candidates as a function of redshift. This figure demonstrates how GLIMPSE significantly reveals fainter galaxies across all redshifts compared to previous *JWST* surveys. With deep observations and gravitational lensing, we pushed the observational limit down by ~ 3 magnitudes in M_{UV} , allowing us to access an important and hitherto unexplored regime of faint galaxies.

5 EFFECTIVE SURVEY VOLUME ESTIMATES

5.1 Completeness Estimates

Before computing the UV luminosity function, we first need to accurately estimate the completeness function of our survey and its associated uncertainties. This process follows the source-plane method described in Atek et al. (2018) and Chemerynska et al. (2024a). The core principle involves implementing mock galaxies, spanning a wide range of properties and redshifts, directly in the source plane reconstructed from the survey image using our cluster mass model. The primary advantage of this approach is the ability to account for all lensing effects simultaneously, including flux magnification,

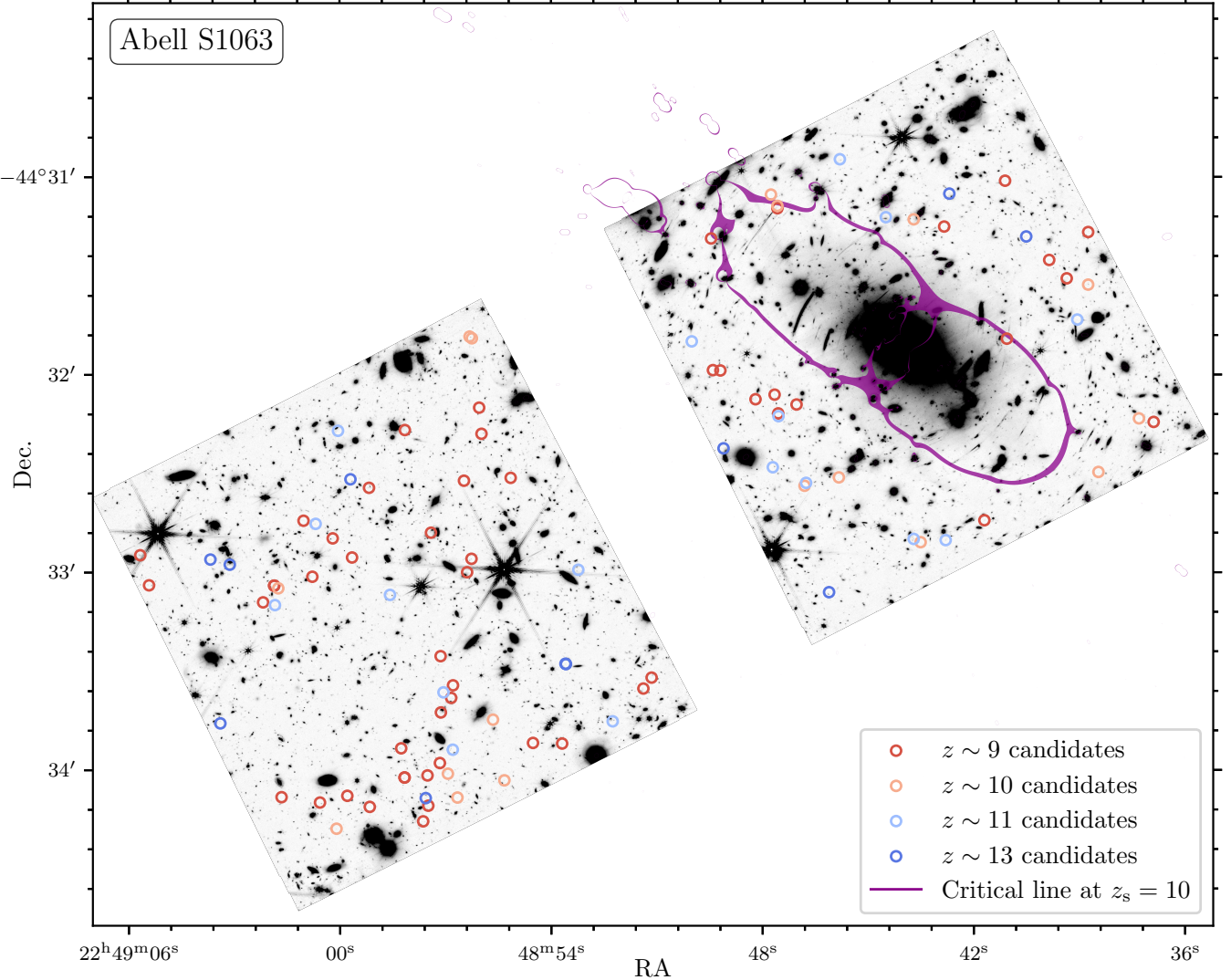


Figure 2. GLIMPSE NIRCam image of AS1063 in the F444W-band showing the positions of our high-redshift candidates in each redshift bin. The critical line for a source at $z_s = 10$ from our lens model (see Section 3) is overlaid in purple.

distortion, geometric deflection, multiple imaging, and the resulting variations in incompleteness due to lensing.

For this procedure, we generated 150,000 mock galaxies at $z = 9 - 12$ and 50,000 across the remaining redshift ranges. These mock galaxies were randomly distributed with redshifts within our redshift range and intrinsic absolute magnitudes ranging from -20 to -10 mag. To ensure realistic source sizes, we applied the size-luminosity relation derived by Yang et al. (2022) for galaxies fainter than -16.5 mag and by Shibuya et al. (2015) for brighter sources. The sources were placed randomly in the source plane, with a higher density in regions of high magnification, to improve the statistical reliability of the completeness function. This adjustment compensates for the tendency of high-magnification regions to be undersampled.

We follow the procedure outlined in Chemerynska et al. (2024a), utilizing SED models generated with BEAGLE (Chevallard & Charlot 2016) to compute synthetic fluxes for the mock galaxies. The templates are based on stellar population models from Bruzual & Charlot (2003) assuming constant star formation, an ionization parameter $\log(U)$ in the range (-4, -1), an SMC extinction law (Pei

1992), and a constant metallicity of $Z = 0.1Z_\odot$, with an extinction in the range $A_V = 0 - 1.25$ applied. The templates were redshifted and normalized to match the observed mock magnitudes in their detection filters (F150W, F200W, F277W), corresponding to the rest-frame UV. Images of the simulated galaxies were then created using GalSim (Rowe et al. 2015), based on their physical properties. These sources were injected into the actual *JWST* bCG subtracted images of the galaxy cluster, placing 100 galaxies at a time to prevent source overlap. Finally, we perform the same photometric measurements and apply the same color-color selection to the full sample of mock galaxies. It is important to note that when multiple images of a mock galaxy are detected, we retain only the brightest candidate. The final completeness function is then computed by comparing the output catalog to the original input catalog, as a function of intrinsic magnitude and redshift. Figure 4 presents the results of our completeness estimates across different redshift ranges. It illustrates the evolution of completeness levels, reaching a maximum of approximately 80%, as a function of intrinsic (unlensed) UV magnitudes and redshifts. For the faintest sources, which require high amplification factors, the

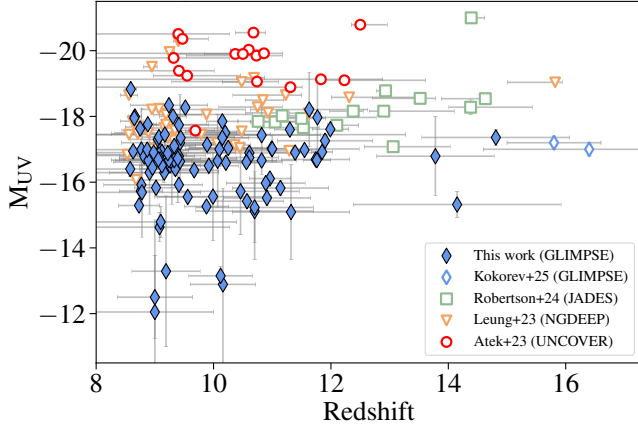


Figure 3. Intrinsic absolute magnitude of the galaxy sample as a function of redshift. The sample from this work is presented in the blue diamonds, together with 2 galaxy candidates from Kokorev et al. (2025) (empty blue diamonds). The uncertainties represent photometric errors along with the propagated magnification uncertainties. For comparison, we also show results from the deepest *JWST* surveys that probe similar redshift range: JADES (Robertson et al. 2024, empty green square), NGDEEP (Leung et al. 2023, empty orange triangle) and the lensed survey UNCOVER (Atek et al. 2023b, empty red circle).

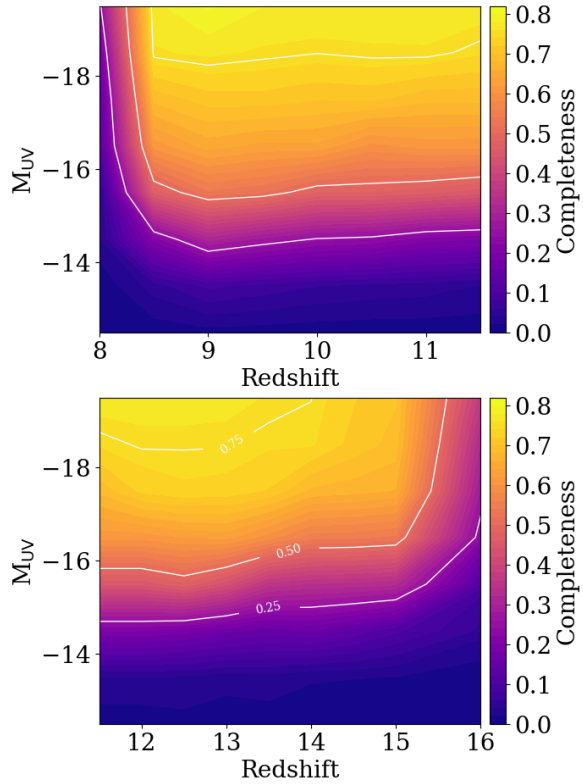


Figure 4. The survey completeness of each redshift range based on the color-color selection (see Section 5.1). Each 2D map shows the completeness fraction (color bar) as a function of both the intrinsic magnitude M_{UV} and the redshift. The completeness reaches a maximum of around 80% near magnitudes $M_{\text{UV}} > -18$ mag and at the center of the redshift selection function. The lowest levels of completeness are for galaxies fainter than $M_{\text{UV}} = -13$ mag, which have less than 10% completeness.

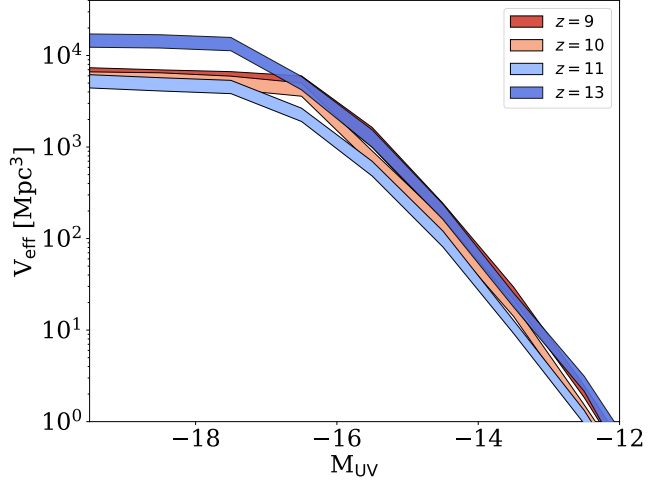


Figure 5. The effective GLIMPSE survey volume through the AS1063 lens as a function of the intrinsic (de-lensed) absolute magnitude. Each curve represents the cumulative volume estimate at a given redshift and M_{UV} , based on the lensing-corrected area, the redshift selection function, and the completeness function (cf. Figure 4). The total survey volume ranges from $\approx 8 \times 10^3 \text{ Mpc}^3$ at $z = 9$ to $19 \times 10^3 \text{ Mpc}^3$ at $z = 13$

completeness drops to just a few percent, primarily due to the limited surface area with high magnification.

5.2 Survey Volume Estimates

The effective volume is determined by the comoving maximal volume, which is distorted by gravitational lensing, multiplied by the completeness function (Atek et al. 2018). The comoving volume depends on the area associated with a specific magnification at a given redshift. We calculate the surface area corresponding to the magnification at a given redshift, as well as the minimal magnification required for a galaxy of a certain magnitude to be detected. The surface area is determined by summing the cumulative area over regions where the magnification exceeds the minimal magnification. The total area of the cluster primarily establishes the maximum volume, as the surface area becomes significantly smaller at progressively higher magnifications. The resulting effective volume for each redshift bin over the intrinsic absolute magnitude is shown in Figure 5.

In addition to the uncertainties in the effective volume, we account for other sources of uncertainty when calculating the galaxy number density in each magnitude bin of the luminosity function. First, we estimate the Poisson confidence intervals following Gehrels (1986), which accounts for small-number statistics. Second, we compute the fractional error due to cosmic variance for each magnitude bin and redshift, using the corresponding lensing-corrected volume. To estimate cosmic variance, we employ the calculator from Trapp & Furlanetto (2020), resulting in $CV = 34 - 50\%$. Finally, we account for all uncertainties affecting the intrinsic magnitudes of galaxies, including those arising from magnification, photometric measurements, and photometric redshift estimates. To incorporate all these uncertainties into our binning scheme, we use Monte Carlo simulations that allow galaxies to shift between bins based on their uncertainty distributions. This approach has the advantage of robustly capturing variations due to the arbitrary choice of bin positions and sizes.

6 THE ULTRAVIOLET LUMINOSITY FUNCTION

After selecting the high- z candidates, we are now ready to compute the UV luminosity function. In order to optimize the number of galaxies in each bin at each redshift, we divide the sample into four redshift sub-samples: $z = 8.5 - 9.5$, $9.5 - 10.5$, $10.5 - 11.5$ and $11.5 - 15$ (centered on $z = 9, 10, 11, 13$; see Tab. 1). To compute the UVLF, we additionally adopt magnitude bins ranging from -18.5 mag to -12.5 , with a bin width of Δ mag = 1. The UV luminosity function at each redshift bin is computed as follows:

$$\phi(M_i) dM_i = \frac{N_{\text{obj},i}}{V_{\text{eff}}(M_i)} \quad (3)$$

where $N_{\text{obj},i}$ represents the number of galaxies in each magnitude bin and $V_{\text{eff}}(M_i)$ denotes the effective volume in the i^{th} bin of absolute UV magnitude M_i .

6.1 The ultra-faint-end of the UV luminosity function at $z > 9$

Our derived UVLF at redshifts above $z = 9$ extends previous estimations into a previously unexplored regime, where we are also able to constrain the faint-end of the luminosity function for the very first time. These constraints are critical for understanding the abundance and properties of faint galaxies in place in this early cosmic epoch. Furthermore, they provide valuable insights into the processes governing galaxy formation and evolution in the first billion years of cosmic history.

In Figure 6, we plot the UVLF determinations at each redshift interval, and provide the best-fit relation at each redshift, including previously published results for the bright end. The derived UVLF data points are provided in Table 1.

Recently, numerous studies have investigated the UVLF at $z > 8$ using *JWST* observations (e.g., Adams et al. 2024; Bouwens et al. 2023; Casey et al. 2024; Castellano et al. 2023; Chemerynska et al. 2024a; Donnan et al. 2024; Finkelstein et al. 2024; Harikane et al. 2024a; Leung et al. 2023; Pérez-González et al. 2023; Willott et al. 2024). Most of these studies have provided robust constraints on the bright end of the LF at high-redshift, revealing that it is better described by a double power law (DPL) rather than the classical Schechter function, since the latter underestimates the numbers of observed bright galaxies. This important result represents one of the most unexpected findings from the initial years of *JWST* operations: that the high number density of observed UV-bright galaxies at $z > 9$ exceeds pre-*JWST* theoretical predictions. We fit our results for the UVLF with a double power law function:

$$\phi(M) = \frac{\phi^*}{10^{0.4(M-M^*)(\alpha+1)} + 10^{0.4(M-M^*)(\beta+1)}} \quad (4)$$

where ϕ^* is the number density normalization of the LF, M^* is the characteristic magnitude, that separates the bright and faint-end distributions, α is the faint-end slope, and β is the bright-end slope. Our sample primarily consists of faint objects ($M_{\text{UV}} > -18.5$), enabling us to accurately constrain the faint-end of the luminosity function.

Since our survey primarily probes the faint regime and a small volume, we rely on bright-end data points from the literature that analyzed wide-area survey data. In our fitting procedure, we incorporate results from the Adams et al. (2024) and Donnan et al. (2024) studies, which derive the UVLF over the same redshift range as our work using a compilation of public surveys. Given the significant dispersion in the bright-end UVLF measurements at $z = 11.5 - 15$ amongst different studies, we include multiple datasets in our fit for this redshift range from Adams et al. (2024); Donnan et al. (2024); Finkelstein et al. (2024); Robertson et al. (2024). Furthermore, to

ensure the robustness of our faint-end fit, we exclude the lowest luminosity bin (-12.5 mag) due to its limited completeness ($\sim 10\%$).

To determine the best-fit parameters and their uncertainties, we perform Markov Chain Monte Carlo (MCMC) simulations. The characteristic magnitude (M^*), the faint-end slope α , the bright-end slope β , and the number density normalization ϕ^* are left as free parameters in all redshift bins. All the values of the best-fit parameters for the DPL function at each redshift are summarized in Table 2.

The overall shape of the luminosity function, combining our results with previous bright-end determinations, is well characterized by a DPL function. Thanks to the combination of ultra-deep imaging and gravitational lensing, our study pushes the luminosity frontier to extremely faint magnitudes. This allows us to provide the first estimates on the very faint-end of the high-redshift UVLF, down to $M_{\text{UV}} \approx -14$, on average. The best-fit UVLF parameters using GLIMPSE data at various redshifts are presented in Table 2. We observe a slow decrease in ϕ^* as a function of redshift, from $\log(\phi^*/\text{Mpc}^{-3} \text{ mag}^{-1}) = -4.01 \pm 0.04$ at $z = 8.5 - 9.5$ to $\log(\phi^*/\text{Mpc}^{-3} \text{ mag}^{-1}) = -4.70 \pm 0.20$ at $z = 11.5 - 15$. This slow evolution of the GLIMPSE data directly mimics the recent *JWST* findings (Finkelstein et al. 2024; Adams et al. 2024; Willott et al. 2024; Donnan et al. 2024), which reported a more modest evolution of the bright end of the UVLF between $z = 8 - 15$. Figure 7 combines the UVLFs derived at different redshifts. While the LF normalization decreases slightly with increasing redshift, the faint-end slopes remain nearly constant from $\alpha = -2.01 \pm 0.20$ at $z = 8.5 - 9.5$ to $\alpha = -2.10 \pm 0.19$ at $z = 11.5 - 15$. This absence of strong evolution is also consistent with the recent findings of Pérez-González et al. (2023) wherein using deep NIRCam observations of the parallel field of the MIDIS survey (Östlin et al. 2024), they investigate the UVLF across $M_{\text{UV}} = -20$ to -17 mag at $z = 9 - 12$. The faint-end slope varies from $\alpha = -2.30^{+0.16}_{-0.24}$ at $z = 9$ to $\alpha = -2.19^{+0.26}_{-0.39}$, consistent within 1σ uncertainties with our derived values, and also indicating slow evolution. While surveys such as CEERS and PRIMER primarily focused on the bright end of the luminosity distribution at these redshifts, deeper surveys like the JADES Origins Field (JOF) and NGDEEP have used significantly longer integration times to probe the population of fainter galaxies. In particular, Leung et al. (2023) present a DPL fit to the UVLF measured at $z = 8.5 - 12$ in the NGDEEP field, finding a slow evolution in the LF from $z = 9$ to $z = 11$ and that the faint-end slope varies from $\alpha = -2.5 \pm 0.4$ to $\alpha = -2.2 \pm 0.2$, which is statistically consistent with no variation. Using observations from the deepest JADES field, Robertson et al. (2024) derived the UVLF at $z = 12 - 14$, adopting a Schechter function form, and found that the LF normalization, ϕ^* , decreased by a factor of ≈ 2.5 moving from $z = 12$ to $z = 14$, which is more pronounced than the results of Leung et al. (2023). Additionally, in the same field, Whitler et al. (2025) explored the UVLF at $z > 9$ for UV luminosities of $-21 < M_{\text{UV}} < -17$ mag. They utilize both the Schechter function and DPL fitting function forms, determining a steep faint-end slope of $-2.5 < \alpha < -2.3$ at redshifts $z = 9 - 16$.

In Figure 8 we summarize the evolution of α , M^* and ϕ^* over a wide redshift range by comparing our results with a compilation of results from the literature at lower redshifts (Wyder et al. 2005; Moutard et al. 2020; Bouwens et al. 2022). Consistent with previous studies, the characteristic magnitude, M^* , plateaus at approximately -20.7 mag. This value is somewhat lower than earlier estimates for $z = 5 - 9$, primarily due to differences in parametrization between the Schechter function and the DPL function. Notably, Bowler et al. (2020), assume a DPL function to model the luminosity function, also report lower values for M^* . Similar trends are observed for the faint-end slope, which evolves rapidly up to $z \sim 8$, and stabilizes around

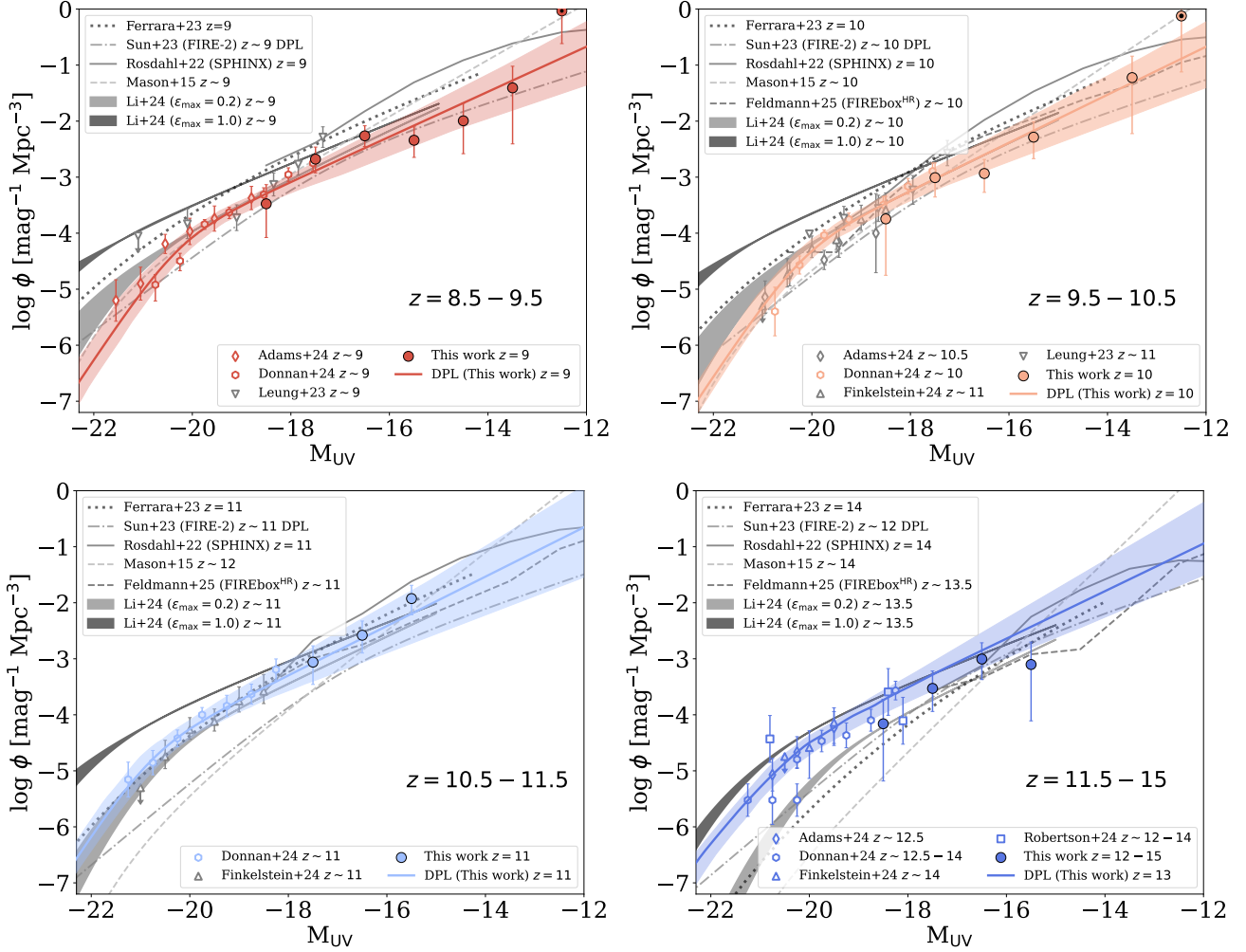


Figure 6. JWST’s GLIMPSE of the ultra faint-end of the UV Luminosity function at $z > 9$. Each panel presents our UVLF determination at a given redshift, alongside literature results at the bright-end. **Top-left:** The UVLF at $z = 9$ shown as red circles with associated 1σ uncertainties (the dark circle denotes the faintest bin, where the completeness is less than $\sim 10\%$). Literature results are shown with various grey symbols (cf. legend) from Adams et al. (2024); Donnan et al. (2024); Leung et al. (2023). The red line represents the best-fit double power law relation, which includes our results at the faint-end and the data points of Donnan et al. (2024) and Adams et al. (2024) at the bright end. The red shaded region denotes the 1σ uncertainty of the best-fit. **Top-right** same as the previous panel but for $z = 10$ and GLIMPSE results are shown in orange, including data from Donnan et al. (2024) at the bright-end. **Bottom-left** same as previous but for $z = 11$. Our results are shown in light blue. **Bottom-right** same as previous panels, but for the redshift range $z = 13$. Here, the fit is performed on data points from various literature results at the bright end (Robertson et al. 2024; Finkelstein et al. 2024; Adams et al. 2024; Donnan et al. 2024) in addition to our GLIMPSE data points at the faint-end. Several theoretical determinations are represented in each of the panels and include the SPHINX simulations (Rosdahl et al. 2022), the FIRE-2 simulations (Sun et al. 2023), the FIREbox^{HR} simulations (Feldmann et al. 2025), models from Ferrara et al. (2023), Mason et al. (2015) and Li et al. (2024).

$\alpha \sim -2.1$ at $z > 9$. Lastly, while there is a pronounced evolution in ϕ^* , we do not detect an “acceleration” for $z > 10$. Such acceleration has been suggested to align with the evolution of the underlying dark matter halo function, which would indicate a constant star formation efficiency in these early galaxies (Mason et al. 2015; Oesch et al. 2018; Tacchella et al. 2018; Sabti et al. 2022).

We also examined how the predicted number of galaxies changes with varying faint-end slopes Bouwens et al. (2022). In Figure 9, we present the magnitude distribution of our sample at each redshift, together with the predicted values of the faint-end of UVLF. This visually shows what faint-end slope reproduces best the observed distribution. The faint-end slope appears to be between -2.0 and -2.2 , which is consistent with our findings from the UVLF. Given that our fit is based on our data as well as other studies, it is clear that

slight variations between observed numbers and those predicted by the faint-end slope can occur. This figure indicates that values of the faint-end around $\alpha < -2.3$, similar to the values reported by Whitler et al. (2025), would lead to an overestimation of the number of sources observed in our field. For example, at redshift $z = 10$, using the DPL parameters from previously mentioned paper with $\alpha = -2.6$, the model predicts approximately $n = 4 \pm 1, 18 \pm 4, 65 \pm 10$ and 51 ± 8 sources across the absolute magnitude range of -18.5 to -15.5 mag. Similarly, at $z = 14$, a DPL fit with $\alpha = -2.42$, also from the same study, would predict $n = 4 \pm 1, 16 \pm 3, 22 \pm 4$, and 20 ± 4 sources across the same magnitude range. All of these predictions overestimate our detected number counts.

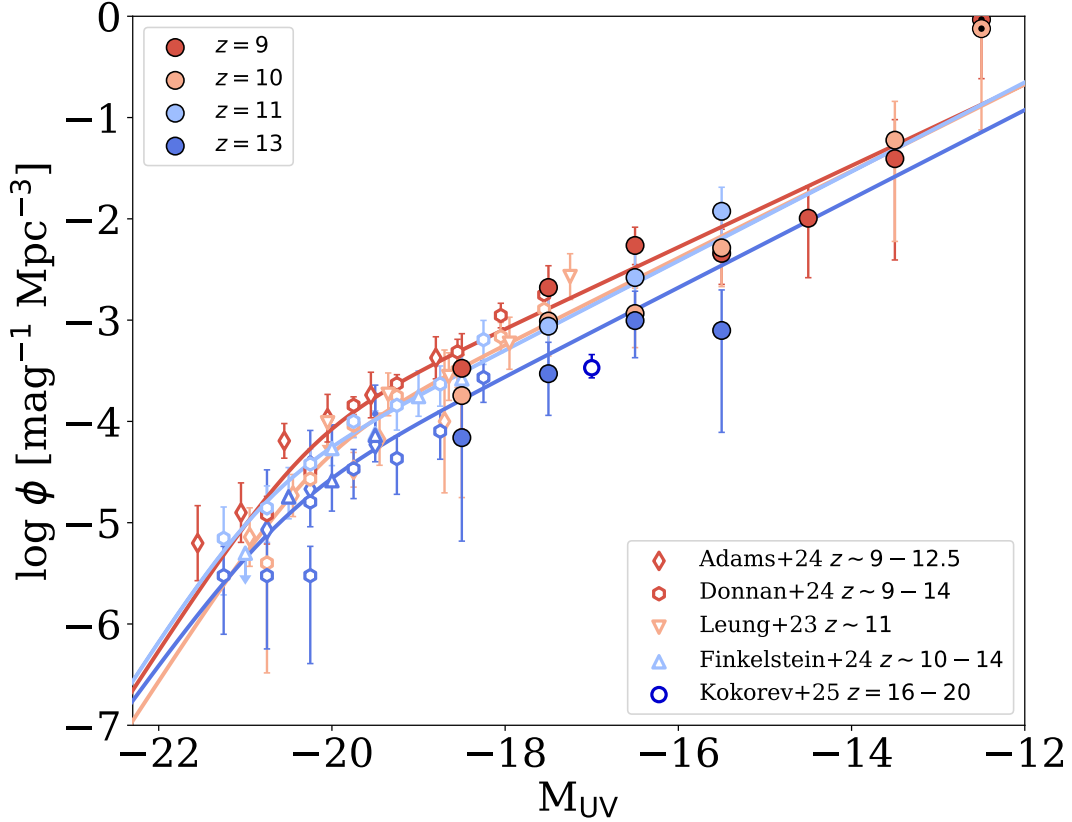


Figure 7. The evolution of the faint-end of the UV luminosity function through Cosmic Dawn. For each redshift, our UVLF points are shown with circles, while the best-fit DPL relation is represented with a solid line. For each redshift, literature results are shown with different symbols, but with the same color as our data points.

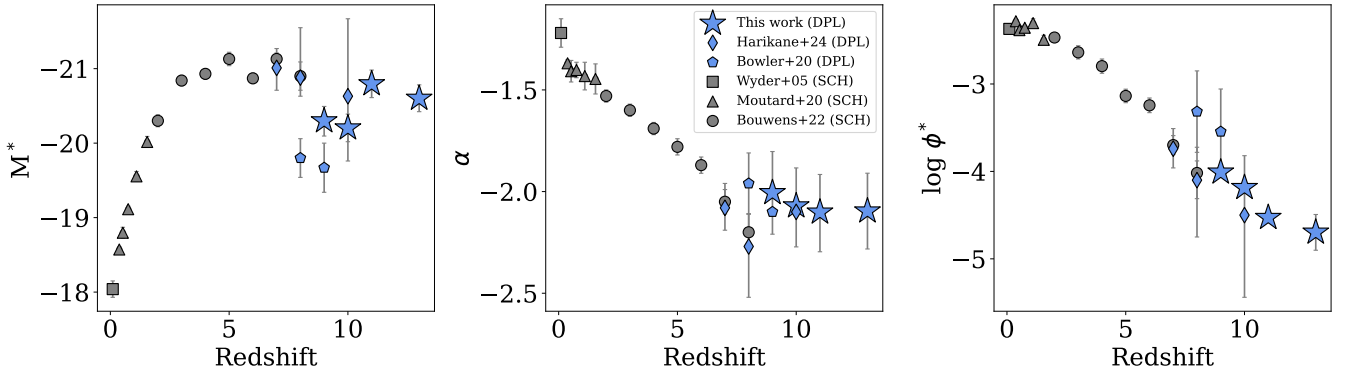


Figure 8. The evolution of the characteristic magnitude (M^*), the faint-end slope (α) and the normalization (ϕ^*) with redshift. Our results, which are based on a DPL parametrization of the LF, are presented as blue stars. In contrast, the grey squares, triangles and circles represent constraints from previous studies at $z = 0.1 - 8$: Wyder et al. (2005), Moutard et al. (2020), and Bouwens et al. (2022), respectively, which were all derived assuming a Schechter function (SCH). We also include results of DPL parametrization for the LF from Bowler et al. (2020, blue pentagons) at $z = 8$ and $z = 9$, and Harikane et al. (2024a, blue diamonds) at $z = 7 - 10$.

6.2 Implications for theoretical models

Probing the fainter part of the UV luminosity function at $z > 9$ offers, for the first time, critical tests for galaxy formation models that have not been previously tested with such a constraint. For each of the UVLFs shown in Figure 6, we compare to both pre-*JWST* and the most recent *JWST*-informed theoretical predictions. Since most pre-*JWST* models underestimate the bright end of the luminosity function

(e.g., Castellano et al. 2023; Chemerynska et al. 2024a; Donnan et al. 2024; Austin et al. 2023), and are based on the assumption of a Schechter function form for the UVLF, they are likely to overestimate the slope at the faint-end. This is the case, for instance, with the model of Mason et al. (2015), which shows a much steeper faint-end slope than our currently derived constraints. The model closely tracks the evolution of the dark matter halo mass function, and assuming a redshift-independent star formation efficiency and mass-to-light

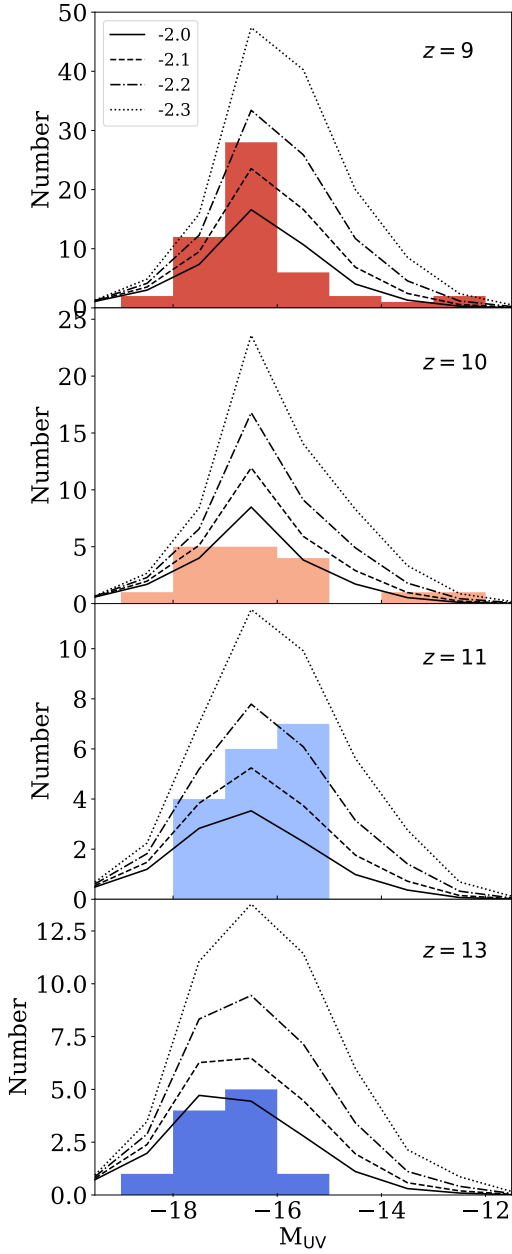


Figure 9. The number of sources as a function of magnitude at redshift from 9 to 15 (from top to bottom). The solid, dashed, dot-dashed, and dotted lines represent the predicted number of sources per bin for different values of the faint-end slope α . Results show that very steep faint-end values tend to overestimate the number of sources, while α values in the range of -2.0 to -2.3 provide good constraints on the faint-end of the UVLF.

ratio. It is calibrated using observations at a specific redshift of around $z \approx 5$ and predicts a progressive steepening of the faint-end slope, reaching $\alpha = -3.5$ by $z = 16$. Consequently, while the model aligns well with the observed LF at $z \sim 10$, it significantly overestimates the abundance of faint galaxies and underestimates the number of bright galaxies at higher redshifts. Based on our results, the steepening of the faint-end slope observed at $z < 9$ appears to slow down significantly at $z > 9$. Our finding highlights the overall discrepancy between pre-JWST predictions—largely based on extrapolations of the redshift evolution of the faint-end slope—and JWST observations.

To reconcile the models with the lack of evolution in the bright

Table 1. Binned ultraviolet luminosity function at $9 < z < 15$. Column M_{UV} shows the bin in absolute UV magnitude. Column N_{obj} indicates the number of objects within each magnitude bin, and Column $\log(\phi)$ presents the number density of these objects, along with associated uncertainties in the number density.

M_{UV}	N_{obj}	$\log(\phi)$ [mag $^{-1}$ Mpc $^{-3}$]
$8.5 < z < 9.5$		
-18.5	2	$-3.48^{+0.34}_{-0.60}$
-17.5	12	$-2.68^{+0.21}_{-0.25}$
-16.5	28	$-2.26^{+0.18}_{-0.19}$
-15.5	6	$-2.34^{+0.24}_{-0.31}$
-14.5	2	$-1.99^{+0.32}_{-0.59}$
-13.5	1	$-1.41^{+0.39}_{-1.00}$
-12.5	2	$-0.03^{+0.31}_{-0.58}$
$9.5 < z < 10.5$		
-18.5	1	$-3.74^{+0.40}_{-1.01}$
-17.5	5	$-3.01^{+0.26}_{-0.35}$
-16.5	5	$-2.93^{+0.25}_{-0.34}$
-15.5	4	$-2.29^{+0.27}_{-0.38}$
-13.5	1	$-1.22^{+0.38}_{-1.00}$
-12.5	1	$-0.12^{+0.38}_{-1.00}$
$10.5 < z < 11.5$		
-17.5	4	$-3.06^{+0.29}_{-0.40}$
-16.5	6	$-2.58^{+0.25}_{-0.32}$
-15.5	2	$-1.93^{+0.24}_{-0.29}$
$11.5 < z < 15$		
-18.5	1	$-4.16^{+0.44}_{-1.02}$
-17.5	4	$-3.53^{+0.31}_{-0.41}$
-16.5	5	$-3.00^{+0.29}_{-0.37}$
-15.5	1	$-3.01^{+0.40}_{-1.01}$

end of the LF at $z > 9$, [Ferrara et al. \(2023\)](#) proposed that the unusual brightness of these sources could be explained by a lack of dust attenuation. This model (dotted line in Figure 7) aligns well with the observed LF at $z \sim 11 - 12$. However, the model exhibits a significantly stronger redshift evolution compared to our GLIMPSE observations. This results in an overestimate of the galaxy number density at $z = 9$ and a substantial underestimate of the LF at $z > 12$ especially at the bright end, where dust attenuation is expected to have a more pronounced impact.

Similarly, stochastic star formation histories have been suggested as a possible explanation for the high number density of bright galaxies. Indeed, initial JWST observations have provided empirical evidence supporting bursty star formation histories in early galaxies ([Strait et al. 2023](#); [Looser et al. 2023](#); [Dressler et al. 2024](#); [Ciesla et al. 2024b](#); [Dome et al. 2024](#); [Endsley et al. 2024](#)). Significant variations in the star formation rate can cause lower-mass galaxies to experience spikes in UV emission, pushing them to the bright end of the luminosity function. Different implementations of this scenario have been explored, yielding contrasting results. [Muñoz et al. \(2023\)](#) and [Shen et al. \(2023\)](#) explored how adding a scatter to UV magnitudes of individual galaxies affects the UVLF, finding that in the context of Λ CDM, a scatter of $\sigma_{\text{UV}} \gtrsim 1.8$ magnitudes is needed to reproduce the UV excess observed with the JWST at $z \gtrsim 9$. Simulation works exploring this scatter also find highly differing results. [Sun et al. \(2023\)](#) find that scatter arising from bursty SFHs in their FIRE simulations is essential and sufficient to reproduce the observed UV excess, while [Pallottini & Ferrara \(2023\)](#) find

Table 2. The best-fitting parameters are derived for DPL fits at each redshift bin. The star formation rate density (ρ_{SFR}) is calculated by integrating down to $M_{\text{UV}} = -16$ mag.

z	$\log(\phi)$ [mag $^{-1}$ Mpc $^{-3}$]	M^* [mag]	α	β	$\log(\rho_{\text{UV}})$ [ergs s $^{-1}$ Hz $^{-1}$ Mpc $^{-3}$]	$\log(\rho_{\text{SFR}})$ [M $_{\odot}$ yr $^{-1}$ Mpc $^{-3}$]
8.5-9.5	$-4.01^{+0.04}_{-0.04}$	$-20.30^{+0.19}_{-0.20}$	$-2.01^{+0.20}_{-0.19}$	$-4.30^{+0.21}_{-0.21}$	25.37 ± 0.44	-2.57 ± 0.44
9.5-10.5	$-4.19^{+0.06}_{-0.06}$	$-20.20^{+0.19}_{-0.18}$	$-2.07^{+0.19}_{-0.19}$	$-4.31^{+0.19}_{-0.19}$	25.20 ± 0.44	-2.74 ± 0.44
10.5-11.5	$-4.53^{+0.01}_{-0.01}$	$-20.80^{+0.19}_{-0.18}$	$-2.10^{+0.19}_{-0.19}$	$-4.35^{+0.19}_{-0.19}$	25.19 ± 0.44	-2.75 ± 0.44
11.5-15	$-4.70^{+0.20}_{-0.21}$	$-20.60^{+0.18}_{-0.18}$	$-2.10^{+0.19}_{-0.19}$	$-4.00^{+0.20}_{-0.18}$	24.92 ± 0.43	-3.02 ± 0.43

a scatter of only $\sigma_{UV} \sim 0.6$ in their SERRA simulations. In general, simulations are heavily dependent on the adopted resolution as well as assumed sub-grid physics for star formation and feedback, thus their predictions need much more investigation before convergence can be reached on the strength of the scatter. In Figure 6, we observe that the LF from the stochastically star-forming simulations of Sun et al. (2023) is slightly lower than the observations across $z = 9 - 15$, possibly due to a different LF normalization. However, the faint-end shape more closely aligns with observations. These effects may stem from their approach, which combines zoom-in simulations with an extrapolation of the LF from a limited number of dark matter halos to a cosmological volume. In the same plot, we also compare our results with the SPHINX cosmological simulations (Rosdahl et al. 2022), which tend to over-predict the number density of faint galaxies, despite having star-formation and feedback models that yield very stochastic star formation histories (see Katz et al. (2023)).

7 COSMIC UV LUMINOSITY AND SFR DENSITY ACROSS REDSHIFTS 9 TO 15

7.1 The redshift-evolution of the UV luminosity density

We can derive the total UV luminosity density ρ_{UV} of galaxies at all redshifts by integrating the UVLF down to a limiting luminosity set by the galaxy formation physics, or more realistically by observational limits. The limited depth of current *JWST* programs means that they fail to accurately account for the contribution of lower-mass halos to the total UV luminosity density, which is typically integrated down to $M_{\text{UV}} = -17$ mag (Harikane et al. 2022a). The GLIMPSE observations provide a better picture of star formation density and efficiency at early epochs, by accounting for galaxies as faint as $M_{\text{UV}} = -13$ mag. Using the best-fit DPL function at each redshift to our UVLF, we integrate the luminosity functions down to a magnitude limit of $M_{\text{UV}} = -16$ mag. This limit has been adopted to maintain a consistent comparison with previously published results, we also integrate them to the same limit (Adams et al. 2024; Donnan et al. 2024; Harikane et al. 2024a; Finkelstein et al. 2024). The uncertainties were determined using a statistical method. We ran the MCMC algorithm 100 times, with each run perturbing the data points within their error bars and accounting for redshift bin uncertainties. For each set of parameters, we integrated the UVLF fit to calculate the corresponding value of ρ_{UV} . The final value for ρ_{UV} is the average of these 100 calculations, and its uncertainty is given by the standard deviation of this distribution.

Figure 10 shows the evolving ρ_{UV} across the redshift range $z = 9 - 13$ and how it compares to a range of results from the literature and the predictions of galaxy formation models. We provide the derived UV luminosity density in Table 2. Our results are consistent with most of the literature between $z = 9$ and $z = 12$ (Donnan et al. 2024; Harikane et al. 2022b; Finkelstein et al. 2024). At higher

redshifts, the derived ρ_{UV} exceeds most determinations, with the exception of Finkelstein et al. (2024). Whieler et al. (2025) results on the UV luminosity density are higher at all redshifts. Pérez-González et al. (2023) also find a shallower evolution of the SFRD at $z = 8 - 13$, leading to a factor of 10 discrepancy with most models. We obtain a best-fit relation to the redshift-evolution of the ρ_{UV} , $\rho_{\text{UV}} = (2.09^{+0.05}_{-0.12}) \times 10^{28} (1+z)^{-2.94^{+0.06}_{-0.10}}$, that is significantly shallower than most theoretical predictions.

Thanks to unprecedented constraints on the faint-end of the UVLF, we can, for the first time, integrate the UV luminosity density to much fainter magnitudes to account for the contribution of fainter galaxies. A census of star-forming galaxies down to $M_{\text{UV}} = -13$ mag (Figure 11) shows that the faint galaxy population, with magnitudes between $M_{\text{UV}} = -16$ and -13 , contributes approximately 50% of the total UV luminosity density of the Universe across nearly all redshifts beyond $z = 9$.

7.2 The evolution of cosmic SFR density

The UV luminosity density can in turn be converted to the star formation rate density (SFRD), noted ρ_{\star} or ρ_{SFR} , assuming a conversion factor between the UV luminosity and the star formation rate based on stellar population models for a given initial mass function (IMF). In the following, we adopt an SFR conversion factor of $K_{\text{UV}} = 1.15 \times 10^{-28} M_{\odot} \text{yr}^{-1}/\text{erg s}^{-1} \text{Hz}^{-1}$ (Madau & Dickinson 2014a), assuming a Salpeter (1955) IMF. This conversion assumes a constant star formation history, which is a clear simplification given the bursty nature of star formation in high-redshift galaxies, especially in low-mass systems (e.g. Tacchella et al. 2020; Asada et al. 2024; Chemerynska et al. 2024b; Marszewski et al. 2024; Endsley et al. 2024; Looser et al. 2025). Rapid variations in star formation can lead to highly fluctuating UV luminosities that may not accurately reflect the averaged star formation rate (SFR) history of these galaxies. Keeping this caveat in mind, the approach enables comparison with recent *JWST* measurements and theoretical predictions (right axis of Figure 10), using a consistent conversion factor.

A direct comparison of the redshift-evolution of the SFRD with the growth of underlying dark matter halo distribution holds key information about the baryon conversion efficiency, i.e., how effectively gas is converted into stars within halos of different masses and at different epochs (Tacchella et al. 2018). The derived slope of the SFRD-redshift evolution, $\rho_{\text{SFR}} = 2.40^{+0.06}_{-0.14} (1+z)^{-2.94^{+0.06}_{-0.10}}$, is significantly shallower than most models, indicating a more gradual increase in the earliest phases of galaxy formation. While recent models match the observed SFRD at $z = 9$, they diverge at higher redshifts because of a much steeper slope in the SFRD- z relation, significantly under-predicting the SFRD. Our derived star formation rate density (SFRD) at redshift $z = 13$ is approximately 1 to 2 orders of magnitude higher than the predictions made by Mason et al.

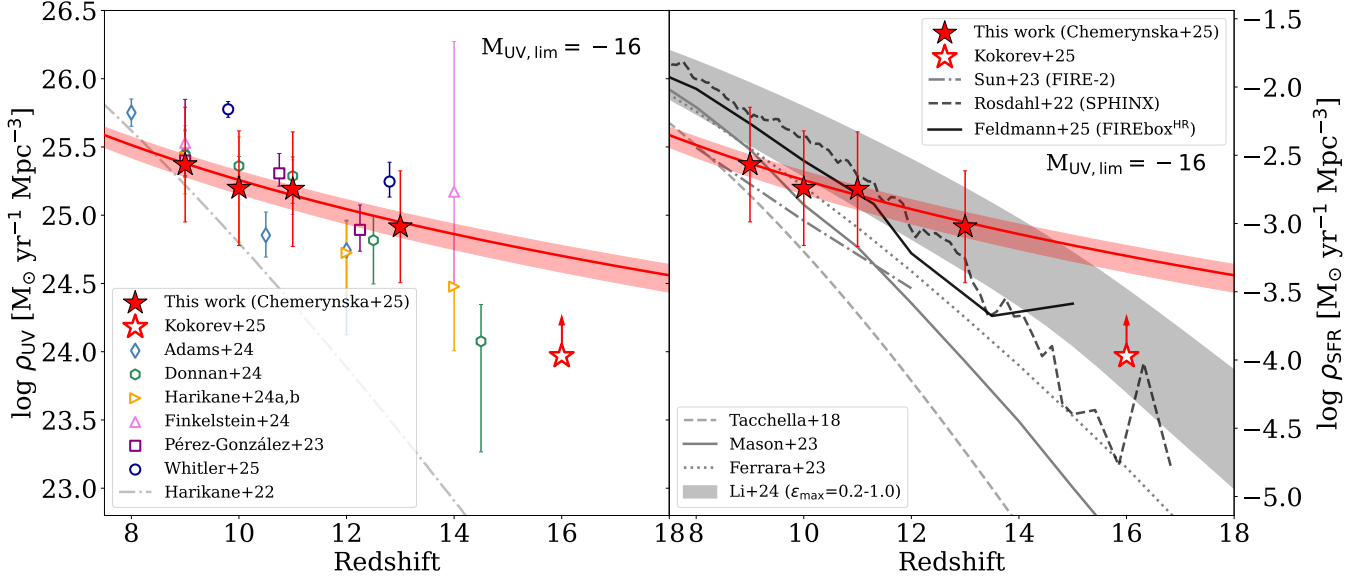


Figure 10. The UV luminosity density (ρ_{UV}) and cosmic star formation rate density (SFRD, ρ_{SFR}) evolution across $z = 9 - 13$. Our ρ_{UV} results, hence ρ_{SFR} , are shown with red stars and derived by integrating each LF down to $M_{\text{UV}} = -16$ mag, including lower limit at $z = 16$ from Kokorev et al. (2025). We then convert the UV luminosity density ρ_{UV} to the SFR density assuming a Salpeter (1955) IMF with conversion factor $K_{\text{UV}} = 1.15 \times 10^{-28} \text{ M}_\odot \text{ yr}^{-1} / \text{erg s}^{-1} \text{ Hz}^{-1}$ (see Table 2). Our best-fit relation to the redshift-evolution of ρ_{UV} is represented by the red line, along with the associated uncertainties represented with the light red region. **Left:** In addition, we plot literature results with open symbols, including Adams et al. (2024); Donnan et al. (2024); Harikane et al. (2024b,a); Finkelstein et al. (2024); Pérez-González et al. (2023); Whitler et al. (2025) and fit to the observed SFRD from Harikane et al. (2022a, grey dash-dotted line). **Right:** We also compare ρ_{UV} to the theoretical predictions of Tacchella et al. (2018, grey dashed line), Mason et al. (2023, dark grey solid line), Ferrara et al. (2023, grey dotted line), Li et al. (2024, grey shaded region), Sun et al. (2023, dark grey dash-dotted line), Rosdahl et al. (2022, black dashed line) and Feldmann et al. (2025, black solid line), for which we adopt the same integration limit.

(2023) and Tacchella et al. (2018), respectively. These results suggest a higher star formation efficiency than what was predicted at $z > 11$, according to both pre- and post-*JWST* models. However, alternative physical scenarios could also explain these findings. The shallower slope of the SFRD relative to the halo mass function may be attributed to an evolving stellar mass-to-light ratio, which results from a younger stellar population at higher redshifts. Figure 11 illustrates our results as a function of redshift compared to various model predictions, similar to Figure 10, which have also been integrated down to the same magnitude limit of $M_{\text{UV}} = -13$ mag. Despite clear mismatches with the observed luminosity functions at $z > 9$, the models by Mason et al. (2023), SPHINX²⁰ (Rosdahl et al. 2022) and FIREbox^{HR} (Feldmann et al. 2025) predict values close to our determinations. However, the redshift evolution in these models remains too steep. In the following, we provide a detailed comparison between this observational determination and individual models and numerical simulations.

7.3 Comparison to theoretical models

Overall, galaxy formation models require an observational anchor for their calibration. Numerical simulations, for instance, rely on phenomenological recipes to represent physical processes occurring on scales smaller than the numerical resolution. This includes crucial components such as star formation and stellar feedback. This “sub-grid” physics depends on parameters that are adjusted and calibrated against observations to ensure realistic predictions. Several models assume a constant star formation efficiency (Mason et al. 2015; Tacchella et al. 2018; Harikane et al. 2022a) as a function of cosmic time, although a dependence with halo mass can be introduced (Ma-

Table 3. The UV luminosity density and cosmic SFR density integrated down to $M_{\text{UV}} = -13$ mag.

z	$\log(\rho_{\text{UV}})$ [ergs $\text{s}^{-1} \text{ Hz}^{-1} \text{ Mpc}^{-3}$]	$\log(\rho_{\text{SFR}})$ [$\text{M}_\odot \text{ yr}^{-1} \text{ Mpc}^{-3}$]
8.5-9.5	25.60 ± 0.44	-2.34 ± 0.44
9.5-10.5	25.47 ± 0.44	-2.47 ± 0.44
10.5-11.5	25.46 ± 0.44	-2.48 ± 0.44
11.5-15	25.19 ± 0.43	-2.75 ± 0.43

son et al. 2015). In this framework, the cosmic SFR naturally tracks the growth of dark matter halo mass, leading to a rapid decline in the SFRD at $z > 9$. However, our results suggest either an increase in star formation efficiency during the earliest stages of galaxy formation, a modified mass-to-light ratio in these galaxies driven by an evolving IMF (Steinhardt et al. 2023; Harikane et al. 2023), a high dispersion in the $M_\star - M_{\text{UV}}$ relation due to highly stochastic star formation histories (Mason et al. 2023; Muñoz et al. 2023; Shen et al. 2023), feedback-free starbursts (Dekel et al. 2023; Li et al. 2024), or dust-free attenuation (Ferrara et al. 2023). Let us explore each of these in turn.

7.3.1 Star Formation History

Bursty SFHs have recently been explored as a potential explanation for the enhanced UV luminosity density observed at $z > 9$ by *JWST*. In particular, using zoom-in simulations from FIRE-2, Sun et al. (2023) demonstrated that a realistic implementation of stellar feedback naturally results in highly bursty star formation. As shown

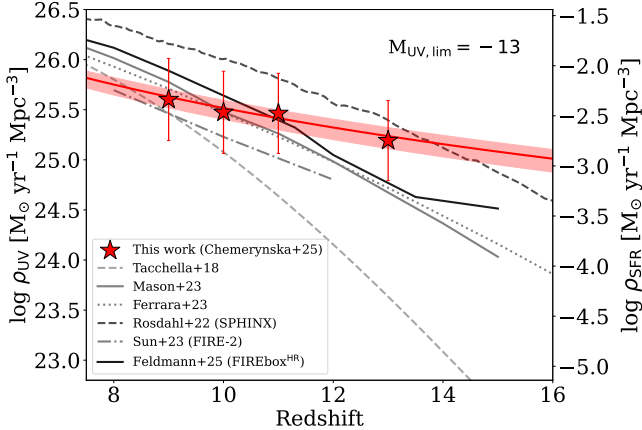


Figure 11. The UV luminosity density and the star formation rate density (SFRD) at $z = 9 - 13$. Our results are shown with the red stars and are based on the integration of the luminosity function at each redshift range, down to an extremely faint-magnitude of $M_{\text{UV}} = -13$ mag. For comparison, we also extend the theoretical models and simulations down to the same integration limit: [Tacchella et al. \(2018\)](#) (grey dashed line), [Mason et al. \(2023\)](#) (dark grey solid line), [Ferrara et al. \(2023\)](#) (grey dotted line), [Sun et al. \(2023\)](#) (FIRE-2) (grey dash-dotted line) and [Rosdahl et al. \(2022\)](#) (black dashed line).

in Figure 6, such rapid variations in star formation can reproduce the overabundance of UV-bright galaxies ($M_{\text{UV}} < -20$) at $z = 9$. However, this approach struggles to match both the fainter end of the LF and its redshift evolution. Consequently, this SFH-driven model shows poor agreement with our measurements when comparing the integrated UV luminosity density as a function of redshift (Figure 10 and 11).

Additionally, the FIREbox^{HR} simulation ([Feldmann et al. 2025](#)) demonstrates good agreement with observational data. Similar to FIRE-2, it reveals that relatively high star formation activity is common in the early Universe. FIREbox^{HR} resolves a significant number of faint, low-mass galaxies. The simulation suggests a non-evolving/weak mass-dependent SFE, which accounts for the increased UV luminosity densities observed at redshifts of $z \sim 6 - 14$. Their results imply that a nearly constant SFE for intermediate-mass halos ($M_{\text{halo}} \sim 10^9 - 10^{11} M_{\odot}$) aligns well with observations, without requiring highly bursty SFHs. This leads to a larger contribution from lower-mass halos at higher redshifts, contributing to the evolution of cosmic UV luminosity density. This contrasts with that of FIRE-2, which attributes the UV-bright galaxy population to rapid bursts of star formation induced by stellar feedback.

Given the uncertainties associated with the conversion from the UV luminosity to the SFR density, we investigate the effects of star formation timescales on the evolution of the SFRD in the SPHINX hydrodynamical simulations and how they compare to our derived constraints. Figure 12 illustrates the SFRD estimated from three distinct indicators in the SPHINX²⁰ simulations ([Rosdahl et al. 2022](#)). The solid line represents the SFRD averaged over 10 Myr, providing a more realistic estimate for bursty SFHs. The dot-dashed line represents the SFRD averaged over the last 100 Myr, which is significantly lower than the SFRD10 line. This highlights the bursty nature of these galaxies during early epochs, resulting in much brighter luminosities compared to values averaged over longer timescales. Additionally, we present the SFRD derived from the UV luminosity in SPHINX, assuming the same conversion factor as used in observations. The dashed curve aligns more closely with SFRD100 at

$z = 9$, but it exhibits a distinct slope as a function of redshift. This divergence primarily arises from the reduction in dust attenuation with increasing redshift.

7.3.2 Feedback-free bursts

Among other scenarios proposed in light of recent *JWST* results, feedback-free starbursts ([Dekel et al. 2023](#); [Li et al. 2024](#)) predict an enhanced star formation efficiency, which can explain the observed overabundance of UV-bright galaxies at $z > 8$. The model defines a density threshold, $n \sim 3 \times 10^3 \text{ cm}^{-3}$, above which the cooling time is shorter than the free-fall time, which leads to an enhancement of the star formation efficiency by a factor $\epsilon_{\text{max}} = 0.2$ to 1. The slow SFRD evolution inferred from our observations means that the SFRD derived at $z = 9 - 10$ is consistent with an efficiency of $\epsilon_{\text{max}} = 0.2$, while the SFRD derived at $z > 12$ requires an efficiency close to $\epsilon_{\text{max}} = 1$ (gray-shaded region in figure 10). In other words, a large increase in the maximum star-formation efficiency with redshift is required for the FFB model to match observations.

7.3.3 Attenuation-free galaxies

Another scenario proposed in [Ferrara et al. \(2023\)](#) relies on outflows that become strong enough above a specific SFR threshold to clear the dust/gas content in galaxies. In this model, the increased unobscured UV luminosity compensates the strong decline in the DM halo mass function, which could explain the overabundance of UV-bright galaxies at $z > 9$. Our galaxies show UV continuum slopes around $\beta \sim -2.3$ to $\beta \sim -2.5$ on average across $z = 9 - 15$ (Jecmen et al. in prep.). These rather blue but not extreme slopes are consistent with low-dust attenuation. In Figure 10 the model captures the SFRD- z evolution of most results up to $z \sim 12$ but falls up to 7 times below our constraints at higher redshifts.

7.4 Caveats

While our results clearly show enhanced star-formation activity at $z > 9$ compared to theoretical models and simulations, they are based on a photometrically selected sample of galaxies. Consequently, uncertainties remain regarding the true redshifts of these sources, as the possibility of low-redshift contaminants, such as dusty star-forming galaxies, cannot be entirely ruled out ([Zavala et al. 2023](#); [Naidu et al. 2022a](#); [Arrabal Haro et al. 2023a](#)). While spectroscopic confirmation is required, the faint population reaches observed magnitudes beyond $m_{\text{AB}} = 30$, mag in F277W filter, making exposure times prohibitive even for *JWST* NIRSpec. An observing strategy that samples this population across different magnitudes could help calibrate the photometric redshifts and, importantly, quantify the contamination rate. Furthermore, a better understanding of the faint dusty star-forming galaxies at $z = 4 - 5$ will also improve the galaxy templates used in photometric redshift estimates ([Barrufet et al. 2023](#); [Weibel et al. 2024](#)). These galaxies can mimic the broad-band colors of high-redshift galaxies and be misidentified as high- z candidates ([Naidu et al. 2022b](#); [Arrabal Haro et al. 2023b](#)).

While the UV luminosity density is a direct measurement, the cosmic star formation rate density (SFRD) is computed by assuming standard calibrations based on a [Salpeter \(1955\)](#) IMF and a constant star formation history. As discussed in Sect. 7.3.1, deviations from these assumptions are expected for early and low-mass galaxies. In the case of bursty star formation, as expected in these galaxies, the UV luminosity may not reliably represent the average SFR over that

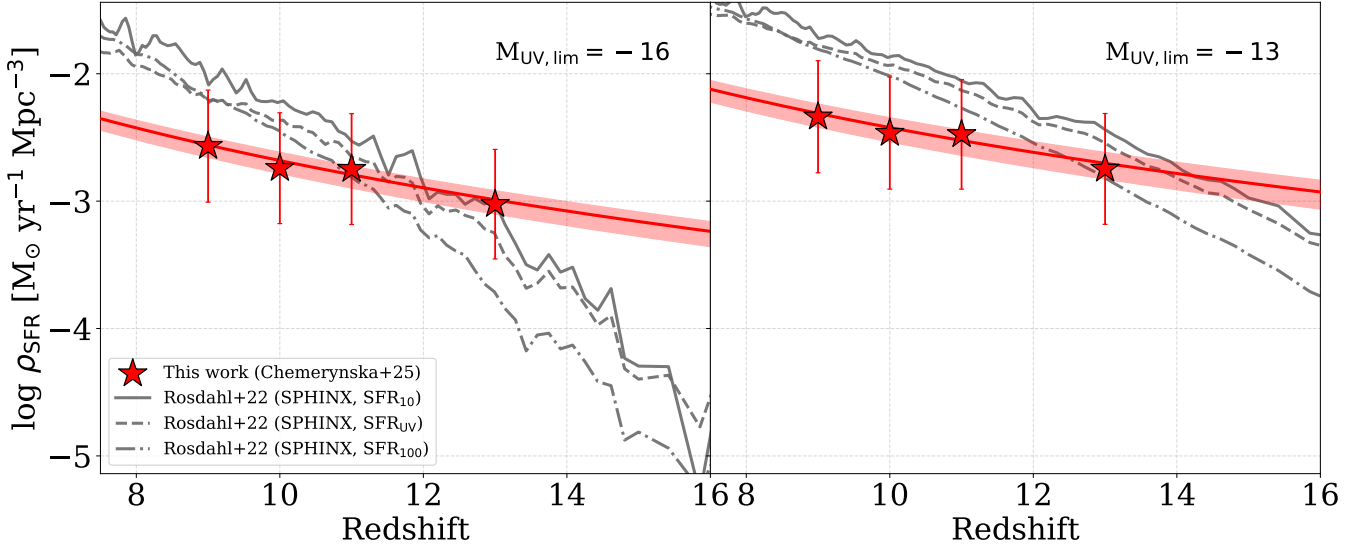


Figure 12. The star formation rate density (SFRD) evolution in the SPHINX simulation (Rosdahl et al. 2022). We compare our results of ρ_{SFR} to different SFRDs derived from SPHINX simulations integrated down to $M_{\text{UV}} = -16$ mag on the left and $M_{\text{UV}} = -13$ mag on the right: averaged on 10 Myr timescale (solid gray line), converted from the UV luminosity density (dashed gray line), and averaged on 100 Myr (gray dash-dotted line).

timescale. This is particularly true for UV-selected galaxies, which are often identified during a recent burst of star formation, typically around 10 Myr, as suggested by recent *JWST* findings (e.g., Loosher et al. 2023). These bursts can contribute to the global enhancement of ρ_{UV} . Additionally, since lower-mass galaxies are more prone to experiencing bursty SFHs (e.g. Atek et al. 2022), such effects can also influence the shape of the UV luminosity function.

Furthermore, variations in the IMF (e.g., a top-heavy IMF) alter the fraction of UV-emitting massive stars, impacting the UV-to-SFR conversion factor (Chon et al. 2022; Steinhardt et al. 2022; Yung et al. 2024; Cueto et al. 2024; Hutter et al. 2024). Additionally, this calibration primarily considers single-star evolution, whereas binary interactions can extend the lifetimes of UV-bright stars, modifying the UV luminosity-SFR relationship, especially in low-metallicity environments. These interactions can lead to a 0.15–0.2 dex higher conversion coefficient (e.g., Ma et al. 2016; Wilkins et al. 2019). Along similar lines, very massive stars (VMS), typically with masses greater than $100 M_{\odot}$, may also impact the UV luminosity distribution for a given stellar population (Crowther et al. 2010; Eldridge & Stanway 2022; Schaefer et al. 2024). Moreover, changing the IMF primarily rescales the mass-to-light ratio (M/L), which in turn affects both stellar masses and star SFRs (Madau & Dickinson 2014b). Therefore, much like the IMF, the star formation history and stellar age are critical factors that directly influence the M/L . For instance, Santini et al. (2023) has revealed that galaxies at redshifts greater than $z > 7$ exhibit a two orders of magnitude range in M/L values for a given luminosity. It is a strong indicator of the broad variety of physical conditions and diverse SFH present in the early galaxies.

All of these measurements are observed quantities and have not been corrected for dust attenuation. Applying such a correction would increase both the UV luminosity and the resulting cosmic SFR density values. However, considering the observed UV continuum slopes (Section 7.3), the dust content in these galaxies is likely low, making the impact of dust attenuation negligible compared to the aforementioned effects (Austin et al. 2023; Narayanan et al. 2024; Saxena et al. 2024; Cullen et al. 2023; Topping et al. 2024b).

An additional factor that could influence our results is the size-luminosity relation, which directly affects the completeness of our calculations. In Section 5.1, we utilized the log-normal distribution derived from Yang et al. (2022) and Shibuya et al. (2015). These studies provide measurements of galaxy size and luminosity at redshifts ($z \sim 4 - 15$). Accurately accounting for galaxy sizes is crucial at faint magnitudes, as smaller faint objects tend to be better recovered (Atek et al. 2018). Consequently, the impact of completeness at the faint-end becomes more significant. Moreover, variations in the size-luminosity relation can significantly affect the slope of the faint-end, potentially making it steeper. Non-parametric size measurements by Curtis-Lake et al. (2016) show no evidence of a positive size-luminosity relation at redshifts $z = 4 - 8$. In this case, the impact of completeness corrections at the faint-end would be more pronounced.

One of the main uncertainties arises from potential field-to-field variations. Given the small volume probed by our survey, particularly in high-magnification regions, cosmic variance could play a significant role, meaning that these properties may not be representative of the large-scale galaxy distribution. This could explain the high number density of galaxies inferred at $z \sim 17$ (Kokorev et al. 2025), while previous equivalently deep blank surveys did not identify any sources at these redshifts. However, when calculating the UV luminosity function, we have accounted for statistical variations due to cosmic variance, and the best-fit UVLF used to derive the SFRD incorporates these uncertainties. Moreover, the higher-than-expected cosmic SFR density is not observed in a single volume at a given redshift, but rather at nearly all redshifts beyond $z = 9$, which contributes to the observed slow redshift evolution.

8 SUMMARY

We use ultra-deep NIRCam imaging of the lensing cluster Abell S1063 to investigate the faintest galaxy population ever observed at $z > 9$. These observations are part of the *JWST* GLIMPSE survey, which has achieved the deepest imaging of the sky to date, offering

an unprecedented view into Cosmic Dawn and the formation and evolution of the earliest galaxies. Using the Lyman-break technique combined with photometric redshifts, we identify a robust sample of 105 galaxy candidates spanning the redshift range $9 < z < 15$. This includes 98 galaxies at $z \sim 9 - 11$ and 7 galaxies at $z \sim 11 - 15$. Notably, some of these sources represent the faintest galaxies ever detected at $z > 9$, with absolute UV magnitudes as faint as $M_{\text{UV}} \approx -13$, corresponding to approximately $0.0003L^*$, the characteristic luminosity at $z \sim 12$ (Table 2).

Using these samples, we compute the UV luminosity function (UVLF) across the redshift range $z = 9$ to $z = 13$. Leveraging extensive simulations and our cluster mass model, we carefully analyzed all lensing effects directly in the source plane to quantify their impact on the survey volume and the resulting UVLFs. Given the small survey volume probed by the GLIMPSE survey, it is primarily sensitive to galaxies fainter than $M_{\text{UV}} = -19$ mag. To account for this, we combine our faint-end data points with results from wide-area surveys in the literature, which probe the bright end of the LF at $M_{\text{UV}} < -18.5$ mag, to provide a comprehensive fit to the UVLF across the full magnitude range.

In the next step, we derive the UV luminosity density, ρ_{UV} , at each redshift by integrating the UV luminosity functions down to $M_{\text{UV}} = -16$ mag. We then convert this luminosity density into the cosmic star formation rate density (SFRD), using the calibration of (Madau & Dickinson 2014b) and assuming a (Salpeter 1955) initial mass function. Our main results are summarized as follows:

- For the first time, we extend the UV luminosity function down to $M_{\text{UV}} \sim -14$ mag at $z > 9$, which is on average 3 magnitudes fainter than any previous *JWST* observations. We observe minimal evolution of the LF with redshift, as indicated by a faint-end slope that varies from $\alpha = -2.01 \pm 0.20$ at $z = 8.5 - 9.5$ to $\alpha = -2.10 \pm 0.19$ at $z = 11.5 - 15$. This lack of strong evolution is consistent with recent deep *JWST* observations that probe brighter galaxies (Pérez-González et al. 2023). Our findings also align with recent *JWST* results showing slow evolution of the bright end of the LF (Bouwens et al. 2023; Finkelstein et al. 2024; Adams et al. 2024; Donnan et al. 2024).

- Similarly, our best-fit relation for the redshift evolution of the cosmic SFR density, ρ_{SFR} , at $z > 9$ follows a slope of $\propto (1+z)^{-2.94}$. This slope is significantly shallower than most theoretical predictions, including the most recent ones informed by early *JWST* results. As a consequence, this leads to a clear underestimate of the theoretical models of the SFRD at redshifts beyond $z \sim 12$.

- For the first time, we integrate the UV luminosity density and cosmic SFRD down to extremely faint luminosities, $M_{\text{UV}} = -13$ mag. As before, the evolution of the SFRD as a function of redshift is slower than predicted by most galaxy formation models. Notably, we find that galaxies fainter than $M_{\text{UV}} = -16$ contribute to more than 50% of the total SFRD in the Universe at redshifts $z = 9 - 15$.

Overall, our findings suggest an enhancement of star formation efficiency at $z > 9$. While the exact physical mechanisms remain uncertain, several plausible scenarios are under investigation. For instance, the observed increase in the UV luminosity density could result from bursty star formation rather than a genuine enhancement of star formation efficiency. In this case, key parameters of the star formation histories—such as the dust cycle and UV dispersion—must be quantified to reconcile the faint-end of the luminosity function and the corresponding evolution of the SFRD at $z > 9$. Additionally, an evolving initial mass function (IMF) could alter the UV-to-SFR conversion, leading to an overestimation of the inferred SFR. Finally, while cosmic variance uncertainties have been incorporated into our

error estimates, field-to-field variations cannot be completely ruled out. Further ultra-deep observations of similarly lensed fields will be critical to confirm this unexpectedly high UV luminosity density in the early Universe.

ACKNOWLEDGMENTS

IC and HA acknowledge support from CNES, focused on the *JWST* mission, and the Programme National Cosmology and Galaxies (PNCG) of CNRS/INSU with INP and IN2P3, co-funded by CEA and CNES. IC acknowledges funding support from the Initiative Physique des Infinis (IPI), a research training program of the Idex SUPER at Sorbonne Université. HA acknowledges support by the French National Research Agency (ANR) under grant ANR-21-CE31-0838. The BGU lensing group acknowledges support by grant No. 2020750 from the United States-Israel Binational Science Foundation (BSF) and grant No. 2109066 from the United States National Science Foundation (NSF), and by the Israel Science Foundation Grant No. 864/23. VK acknowledges support from the University of Texas at Austin Cosmic Frontier Center. AA acknowledges support by the Swedish research council Vetenskapsrådet (2021-05559). This work has received funding from the Swiss State Secretariat for Education, Research and Innovation (SERI) under contract number MB22.00072, as well as from the Swiss National Science Foundation (SNSF) through project grant 200020_207349. This work has made use of the CANDIDE Cluster at the *Institut d’Astrophysique de Paris* (IAP), made possible by grants from the PNCG and the region of Île de France through the program DIM-ACAV+, and the Cosmic Dawn Center and maintained by S. Rouberol. P.N. acknowledges support from the Gordon and Betty Moore Foundation and the John Templeton Foundation that fund the Black Hole Initiative (BHI) at Harvard University where she serves as one of the PIs. This work is based on observations obtained with the NASA/ESA/CSA *JWST* and the NASA/ESA *Hubble Space Telescope* (HST), retrieved from the *Mikulski Archive for Space Telescopes* (MAST) at the *Space Telescope Science Institute* (STScI). STScI is operated by the Association of Universities for Research in Astronomy, Inc. under NASA contract NAS 5-26555.

DATA AVAILABILITY

The data underlying this article are publicly available on the *Mikulski Archive for Space Telescopes*¹ (MAST), under program ID 3293.

APPENDIX A: HIGH-REDSHIFT CANDIDATES

In this section, we provide additional details about the galaxy candidates selected in Section 4. Figure A1 showcases the best-fit SEDs for a representative candidate from each redshift range, derived using two independent codes: BEAGLE and EAZY. While at the highest redshifts, the two codes may differ in attributing the flux excess in the reddest band to either a Balmer break or strong emission lines, they consistently converge on the best-fit redshift solution. This agreement is reflected in the narrow posterior probability distribution of

¹ <https://archive.stsci.edu/>

the redshift. Additionally, we present imaging cutouts of the candidates in each of the nine NIRCam filters, highlighting the Lyman break and their corresponding magnitudes.

REFERENCES

Acebron A., Jullo E., Limousin M., Tilquin A., Giocoli C., Jauzac M., Mahler G., Richard J., 2017, *MNRAS*, **470**, 1809

Adams N. J., et al., 2024, *ApJ*, **965**, 169

Agertz O., Kravtsov A. V., 2015, *ApJ*, **804**, 18

Allard F., Hauschildt P. H., Alexander D. R., Tamai A., Schweitzer A., 2001, *ApJ*, **556**, 357

Arrabal Haro P., et al., 2023a, *arXiv e-prints*, p. arXiv:2303.15431

Arrabal Haro P., et al., 2023b, *ApJ*, **951**, L22

Asada Y., et al., 2024, *MNRAS*, **527**, 11372

Atek H., Richard J., Kneib J.-P., Schaefer D., 2018, *MNRAS*, **479**, 5184

Atek H., Furtak L. J., Oesch P., van Dokkum P., Reddy N., Contini T., Illingworth G., Wilkins S., 2022, *MNRAS*, **511**, 4464

Atek H., et al., 2023a, *MNRAS*, **519**, 1201

Atek H., et al., 2023b, *MNRAS*, **524**, 5486

Austin D., et al., 2023, *ApJ*, **952**, L7

Balestra I., et al., 2013, *A&A*, **559**, L9

Barrufet L., et al., 2023, *MNRAS*, **522**, 449

Beauchesne B., et al., 2024, *MNRAS*, **527**, 3246

Bergamini P., et al., 2019, *A&A*, **631**, A130

Bertin E., Arnouts S., 1996, *A&AS*, **117**, 393

Bogdan A., et al., 2023, *arXiv e-prints*, p. arXiv:2305.15458

Bouwens R. J., et al., 2015, *ApJ*, **803**, 34

Bouwens R. J., Illingworth G., Ellis R. S., Oesch P., Stefanon M., 2022, *ApJ*, **940**, 55

Bouwens R., Illingworth G., Oesch P., Stefanon M., Naidu R., van Leeuwen I., Magee D., 2023, *MNRAS*, **523**, 1009

Bowler R. A. A., Jarvis M. J., Dunlop J. S., McLure R. J., McLeod D. J., Adams N. J., Milvang-Jensen B., McCracken H. J., 2020, *MNRAS*, **493**, 2059

Brammer G. B., van Dokkum P. G., Coppi P., 2008, *ApJ*, **686**, 1503

Bruzual G., Charlot S., 2003, *MNRAS*, **344**, 1000

Calzetti D., Armus L., Bohlin R. C., Kinney A. L., Koornneef J., Storchi-Bergmann T., 2000, *ApJ*, **533**, 682

Carnall A. C., et al., 2023, *MNRAS*, **518**, L45

Carniani S., et al., 2024, *arXiv e-prints*, p. arXiv:2405.18485

Casey C. M., et al., 2024, *ApJ*, **965**, 98

Castellano M., et al., 2023, *ApJ*, **948**, L14

Chabrier G., Baraffe I., Allard F., Hauschildt P., 2000, *ApJ*, **542**, 464

Chemerynska I., et al., 2024a, *MNRAS*, **531**, 2615

Chemerynska I., et al., 2024b, *ApJ*, **976**, L15

Chevallard J., Charlot S., 2016, *MNRAS*, **462**, 1415

Chon S., Ono H., Omukai K., Schneider R., 2022, *MNRAS*, **514**, 4639

Ciesla L., et al., 2024a, *A&A*, **686**, A128

Ciesla L., et al., 2024b, *A&A*, **686**, A128

Crain R. A., et al., 2015, *MNRAS*, **450**, 1937

Crowther P. A., Schnurr O., Hirschi R., Yusof N., Parker R. J., Goodwin S. P., Kassim H. A., 2010, *MNRAS*, **408**, 731

Cueto E. R., Hutter A., Dayal P., Gottlöber S., Heintz K. E., Mason C., Trebitsch M., Yepes G., 2024, *A&A*, **686**, A138

Cullen F., et al., 2023, *MNRAS*, **520**, 14

Curtis-Lake E., et al., 2016, *MNRAS*, **457**, 440

Curtis-Lake E., et al., 2022, *arXiv e-prints*, p. arXiv:2212.04568

Davé R., Anglés-Alcázar D., Narayanan D., Li Q., Rafieferantsoa M. H., Appleby S., 2019, *MNRAS*, **486**, 2827

Dayal P., Ferrara A., 2018, *Phys. Rep.*, **780**, 1

Dayal P., Ferrara A., Dunlop J. S., Pacucci F., 2014, *MNRAS*, **445**, 2545

Dayal P., Rossi E. M., Shiraliolou B., Piana O., Choudhury T. R., Volonteri M., 2019, *MNRAS*, **486**, 2336

Dekel A., Sarkar K. S., Birnboim Y., Mandelker N., Li Z., 2023, *arXiv e-prints*, p. arXiv:2303.04827

Dome T., Tacchella S., Fialkov A., Ceverino D., Dekel A., Ginzburg O., Lapiner S., Looser T. J., 2024, *MNRAS*, **527**, 2139

Donnan C. T., et al., 2024, *MNRAS*, **533**, 3222

Dressler A., et al., 2024, *ApJ*, **964**, 150

Eldridge J. J., Stanway E. R., 2022, *ARA&A*, **60**, 455

Elíásdóttir Á., et al., 2007, preprint, (arXiv:0710.5636)

Endsley R., et al., 2024, *MNRAS*, **533**, 1111

Feldmann R., et al., 2025, *MNRAS*, **536**, 988

Ferrara A., 2024, *A&A*, **684**, A207

Ferrara A., Pallottini A., Dayal P., 2023, *MNRAS*, **522**, 3986

Finkelstein S. L., et al., 2015, *ApJ*, **810**, 71

Finkelstein S. L., et al., 2022, *ApJ*, **940**, L55

Finkelstein S. L., et al., 2024, *ApJ*, **969**, L2

Fujimoto S., et al., 2023, *arXiv e-prints*, p. arXiv:2308.11609

Fujimoto S., et al., 2025, *ApJ*, **989**, 46

Furtak L. J., et al., 2023, *MNRAS*, **523**, 4568

Gatto A., et al., 2017, *MNRAS*, **466**, 1903

Gehrels N., 1986, *ApJ*, **303**, 336

Giavalisco M., 2002, *ARA&A*, **40**, 579

Hainline K. N., et al., 2023, *arXiv e-prints*, p. arXiv:2306.02468

Harikane Y., et al., 2022a, *ApJS*, **259**, 20

Harikane Y., et al., 2022b, *ApJS*, **259**, 20

Harikane Y., et al., 2023, *ApJS*, **265**, 5

Harikane Y., et al., 2024a, *arXiv e-prints*, p. arXiv:2406.18352

Harikane Y., Nakajima K., Ouchi M., Umeda H., Isobe Y., Ono Y., Xu Y., Zhang Y., 2024b, *ApJ*, **960**, 56

Hutter A., Dayal P., Yepes G., Gottlöber S., Legrand L., Ucci G., 2021, *MNRAS*, **503**, 3698

Hutter A., Cueto E. R., Dayal P., Gottlöber S., Trebitsch M., Yepes G., 2024, *arXiv e-prints*, p. arXiv:2410.00730

Kassiola A., Kovner I., 1993, *ApJ*, **417**, 450

Katz H., et al., 2023, *The Open Journal of Astrophysics*, **6**, 44

Kokorev V., et al., 2025, *ApJ*, **983**, L22

Leung G. C. K., et al., 2023, *ApJ*, **954**, L46

Li Z., Dekel A., Sarkar K. C., Aung H., Giavalisco M., Mandelker N., Tacchella S., 2024, *A&A*, **690**, A108

Limousin M., et al., 2024, *arXiv e-prints*, p. arXiv:2409.04584

Liu C., Mutch S. J., Angel P. W., Duffy A. R., Geil P. M., Poole G. B., Mesinger A., Wyithe J. S. B., 2016, *MNRAS*, **462**, 235

Looser T. J., et al., 2023, *arXiv e-prints*, p. arXiv:2306.02470

Looser T. J., et al., 2025, *A&A*, **697**, A88

Lotz J. M., et al., 2017, *ApJ*, **837**, 97

Ma X., Hopkins P. F., Faucher-Giguère C.-A., Zolman N., Muratov A. L., Kereš D., Quataert E., 2016, *MNRAS*, **456**, 2140

Madau P., Dickinson M., 2014a, *ARA&A*, **52**, 415

Madau P., Dickinson M., 2014b, *ARA&A*, **52**, 415

Marszewski A., Sun G., Faucher-Giguère C.-A., Hayward C. C., Feldmann R., 2024, *arXiv e-prints*, p. arXiv:2403.08853

Mashian N., Oesch P. A., Loeb A., 2016, *MNRAS*, **455**, 2101

Mason C. A., Trenti M., Treu T., 2015, *ApJ*, **813**, 21

Mason C. A., Trenti M., Treu T., 2023, *MNRAS*, **521**, 497

McLeod D. J., et al., 2024, *MNRAS*, **527**, 5004

Moutard T., Sawicki M., Arnouts S., Golob A., Coupon J., Ilbert O., Yang X., Gwyn S., 2020, *MNRAS*, **494**, 1894

Muñoz J. B., Mirocha J., Furlanetto S., Sabti N., 2023, *MNRAS*, **526**, L47

Naidu R. P., et al., 2022a, *arXiv e-prints*, p. arXiv:2208.02794

Naidu R. P., et al., 2022b, *ApJ*, **940**, L14

Narayanan D., et al., 2024, *arXiv e-prints*, p. arXiv:2408.13312

Natarajan P., Kneib J.-P., 1997, *MNRAS*, **287**, 833

Oesch P. A., Bouwens R. J., Illingworth G. D., Labbé I., Stefanon M., 2018, *ApJ*, **855**, 105

Östlin G., et al., 2024, *arXiv e-prints*, p. arXiv:2411.19686

Pallottini A., Ferrara A., 2023, *A&A*, **677**, L4

Pei Y. C., 1992, *ApJ*, **395**, 130

Pérez-González P. G., et al., 2023, *ApJ*, **951**, L1

Polletta M., et al., 2007, *ApJ*, **663**, 81

Press W. H., Schechter P., 1974, *ApJ*, **187**, 425

Reddy N. A., et al., 2015, *ApJ*, **806**, 259

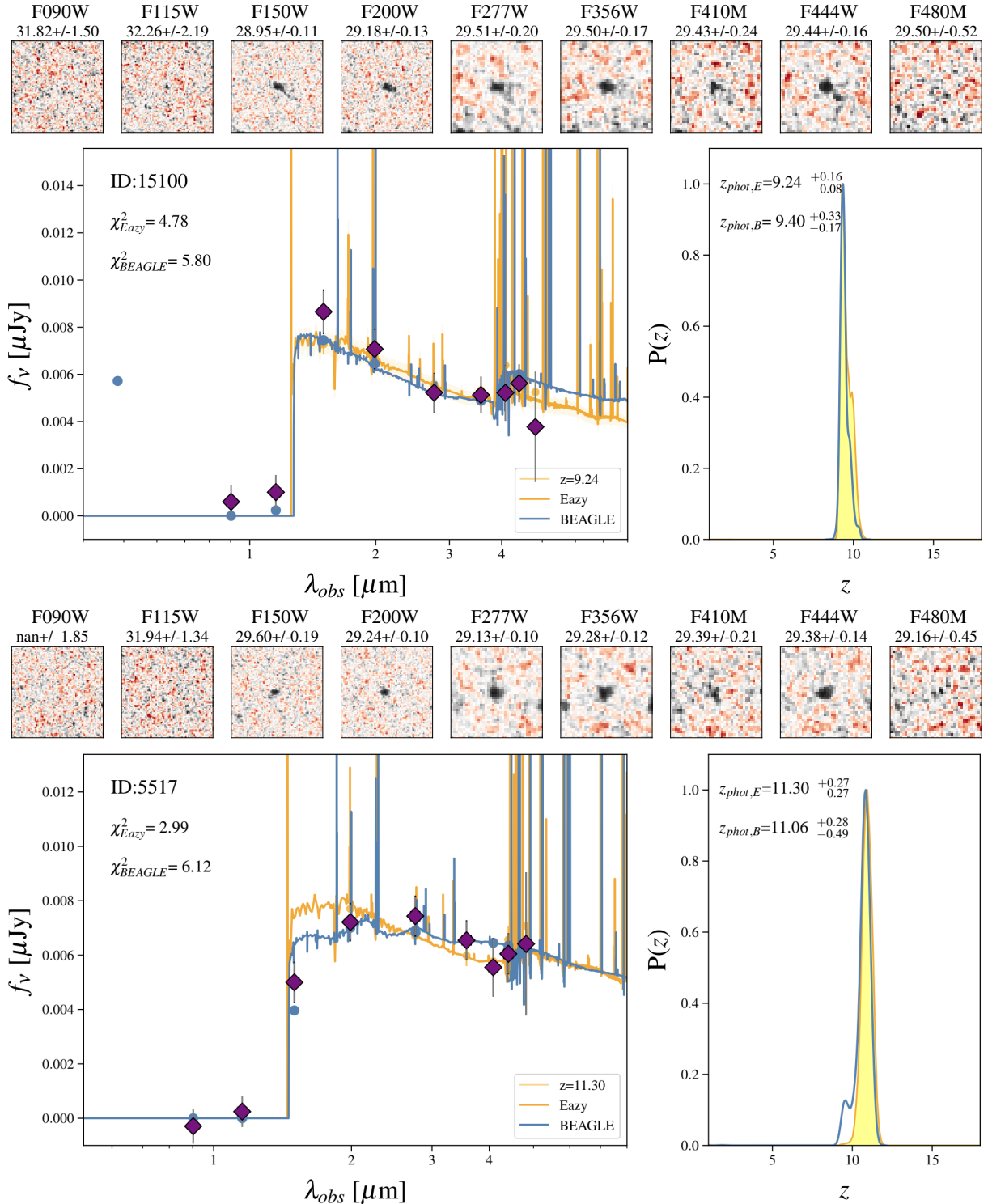


Figure A1. Examples of galaxy candidates at different redshifts, showing NIRCam imaging and best-fit SED solutions. The top row displays cutouts of each candidate across the nine *JWST* filters. The bottom panel features the best-fit SEDs generated by EAZY (orange curve) and BEAGLE (blue curve), along with the object ID and the best-fit χ^2 values from both codes. The purple diamonds represent the observed fluxes, while the orange and blue circles show the best-fit model magnitudes from EAZY and BEAGLE, respectively. On the right panel, the photometric redshift probability distribution functions (PDFs) from both codes are shown, in addition to the best-fit redshift and associated uncertainties.

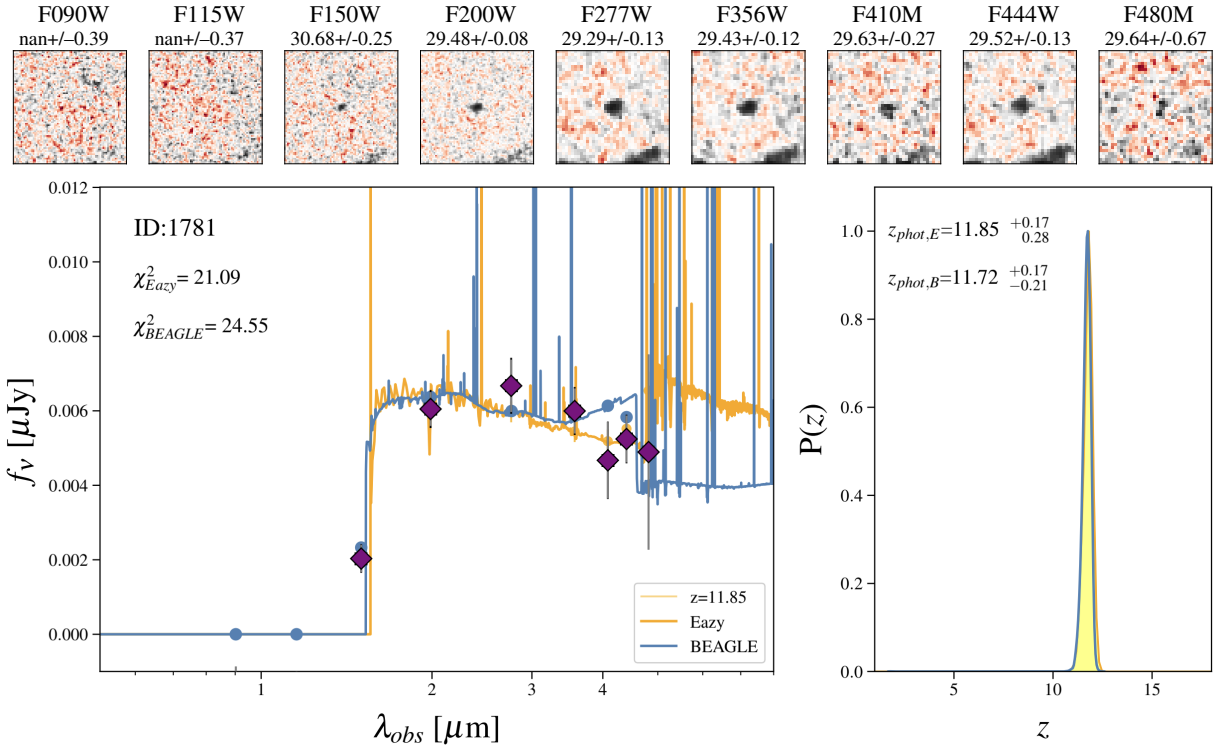


Figure A2. Same as Figure A1

Richard J., et al., 2021, [A&A](#), **646**, A83
 Roberts-Borsani G., et al., 2023, [Nature](#), **618**, 480
 Robertson B., et al., 2024, [ApJ](#), **970**, 31
 Rosdahl J., et al., 2022, [MNRAS](#), **515**, 2386
 Rowe B. T. P., et al., 2015, [Astronomy and Computing](#), **10**, 121
 Sabti N., Muñoz J. B., Blas D., 2022, [Phys. Rev. D](#), **105**, 043518
 Salpeter E. E., 1955, [ApJ](#), **121**, 161
 Santini P., et al., 2023, [ApJ](#), **942**, L27
 Saxena A., et al., 2024, [A&A](#), **684**, A84
 Schaefer D., Guibert J., Marques-Chaves R., Martins F., 2024, [arXiv e-prints](#), p. [arXiv:2407.12122](#)
 Shen X., Vogelsberger M., Boylan-Kolchin M., Tacchella S., Kannan R., 2023, [MNRAS](#), **525**, 3254
 Shibuya T., Ouchi M., Harikane Y., 2015, [ApJS](#), **219**, 15
 Shipley H., et al., 2018, preprint, ([arXiv:1801.09734](#))
 Silva L., Granato G. L., Bressan A., Danese L., 1998, [ApJ](#), **509**, 103
 Springel V., et al., 2005, [Nature](#), **435**, 629
 Steidel C. C., Giavalisco M., Pettini M., Dickinson M., Adelberger K. L., 1996, [ApJ](#), **462**, L17
 Steinhardt C. L., et al., 2020, [ApJS](#), **247**, 64
 Steinhardt C. L., et al., 2022, [ApJ](#), **931**, 58
 Steinhardt C. L., Kokorev V., Rusakov V., Garcia E., Sneppen A., 2023, [ApJ](#), **951**, L40
 Strait V., et al., 2023, [ApJ](#), **949**, L23
 Suess K. A., et al., 2024, [ApJ](#), **976**, 101
 Sun G., Faucher-Giguère C.-A., Hayward C. C., Shen X., Wetzel A., Cochrane R. K., 2023, [ApJ](#), **955**, L35
 Tacchella S., Bose S., Conroy C., Eisenstein D. J., Johnson B. D., 2018, [ApJ](#), **868**, 92
 Tacchella S., Forbes J. C., Caplar N., 2020, [MNRAS](#), **497**, 698
 Topping M. W., et al., 2024a, [MNRAS](#), **529**, 3301
 Topping M. W., et al., 2024b, [MNRAS](#), **529**, 4087
 Trapp A. C., Furlanetto S. R., 2020, [MNRAS](#), **499**, 2401
 Vogelsberger M., et al., 2020, [MNRAS](#), **492**, 5167
 Weaver J. R., et al., 2024, [ApJS](#), **270**, 7
 Weibel A., et al., 2024, [MNRAS](#), **533**, 1808
 Whitler L., et al., 2025, [arXiv e-prints](#), p. [arXiv:2501.00984](#)
 Wilkins S. M., Lovell C. C., Stanway E. R., 2019, [MNRAS](#), **490**, 5359
 Willott C. J., et al., 2024, [ApJ](#), **966**, 74
 Wyder T. K., et al., 2005, [ApJ](#), **619**, L15
 Yang L., et al., 2022, [AJL](#), **938**, L17
 Yung L. Y. A., Somerville R. S., Popping G., Finkelstein S. L., Ferguson H. C., Davé R., 2019, [MNRAS](#), **490**, 2855
 Yung L. Y. A., Somerville R. S., Finkelstein S. L., Wilkins S. M., Gardner J. P., 2024, [MNRAS](#), **527**, 5929
 Zavala J. A., et al., 2023, [ApJ](#), **943**, L9
 Zitrin A., et al., 2015, [ApJ](#), **801**, 44

Table A1. Summary of the full sample of the galaxy candidates at $z \sim 9 - 15$ analyzed in this paper.

ID	RA(J2000)	DEC(J2000)	z_{phot}	$M_{\text{UV}}[\text{mag}]$	μ
5255	342.236847	-44.560589	8.58 ± 0.61	-16.40 ± 0.22	1.29 ± 0.15
48305	342.246552	-44.542870	8.59 ± 0.10	-18.83 ± 0.04	1.37 ± 0.15
13557	342.250854	-44.547131	8.63 ± 0.13	-16.94 ± 0.05	1.32 ± 0.15
56616	342.229797	-44.542038	8.65 ± 0.08	-17.95 ± 0.03	1.52 ± 0.19
12280	342.234436	-44.548862	8.66 ± 0.11	-18.00 ± 0.04	1.39 ± 0.16
30848	342.205872	-44.532963	8.73 ± 0.35	-15.29 ± 0.13	3.21 ± 0.48
3468	342.223724	-44.564442	8.75 ± 0.12	-17.63 ± 0.04	1.34 ± 0.15
31824	342.204987	-44.532993	8.76 ± 0.37	-15.73 ± 0.14	3.37 ± 0.50
3492	342.227173	-44.564388	8.77 ± 3.33	-16.99 ± 1.24	1.31 ± 0.15
52490	342.171326	-44.516994	8.77 ± 0.64	-15.92 ± 0.23	2.34 ± 0.32
60624	342.166107	-44.523674	8.78 ± 3.45	-15.69 ± 1.36	2.94 ± 0.43
6208	342.213135	-44.558884	8.82 ± 0.42	-16.78 ± 0.15	1.44 ± 0.18
1605	342.239563	-44.569675	8.87 ± 0.41	-16.86 ± 0.14	1.24 ± 0.14
11203	342.253265	-44.550365	8.87 ± 0.30	-16.99 ± 0.10	1.29 ± 0.15
4683	342.238068	-44.561813	8.88 ± 0.15	-17.76 ± 0.05	1.28 ± 0.14
7171	342.238098	-44.557068	8.89 ± 0.56	-16.66 ± 0.19	1.31 ± 0.15
2797	342.238190	-44.566078	8.91 ± 3.44	-16.29 ± 1.26	1.26 ± 0.14
5833	342.236633	-44.559528	8.95 ± 0.92	-16.81 ± 0.31	1.30 ± 0.15
40044	342.153748	-44.537327	8.96 ± 0.10	-16.44 ± 0.04	3.46 ± 0.56
14967	342.254303	-44.545643	8.98 ± 1.39	-16.90 ± 0.48	1.31 ± 0.15
57891	342.206085	-44.521862	9.00 ± 0.64	-12.50 ± 1.27	59.90 ± 56.75
69815	342.171112	-44.530312	9.00 ± 4.38	-12.05 ± 2.80	87.20 ± 71.51
36308	342.200836	-44.535419	9.02 ± 0.37	-15.83 ± 0.13	3.52 ± 0.48
1177	342.240173	-44.570992	9.05 ± 0.46	-17.30 ± 0.15	1.23 ± 0.14
72488	342.257782	-44.551109	9.06 ± 0.59	-16.69 ± 0.20	1.27 ± 0.14
9783	342.259094	-44.552521	9.07 ± 0.47	-16.84 ± 0.16	1.26 ± 0.14
12322	342.248566	-44.548744	9.07 ± 0.28	-17.37 ± 0.09	1.32 ± 0.15
37282	342.195984	-44.535862	9.08 ± 1.20	-14.63 ± 0.45	4.97 ± 0.76
1837	342.249146	-44.568836	9.09 ± 0.49	-16.97 ± 0.16	1.22 ± 0.14
10705	342.257782	-44.551113	9.09 ± 0.69	-16.69 ± 0.23	1.27 ± 0.14
56793	342.178528	-44.520859	9.10 ± 1.29	-14.79 ± 0.48	4.56 ± 0.76
2416	342.239655	-44.567123	9.12 ± 0.36	-16.92 ± 0.12	1.25 ± 0.14
38745	342.198151	-44.536610	9.12 ± 0.08	-16.51 ± 0.03	3.75 ± 0.57
37840	342.233521	-44.536118	9.16 ± 0.93	-16.29 ± 0.31	1.61 ± 0.19
14073	342.239227	-44.546658	9.17 ± 1.80	-17.45 ± 0.61	1.38 ± 0.16
54451	342.198242	-44.519318	9.19 ± 0.58	-13.29 ± 2.29	53.32 ± 111.3
41319	342.242310	-44.538002	9.22 ± 0.72	-16.88 ± 0.24	1.45 ± 0.18
12594	342.273621	-44.548538	9.24 ± 0.66	-18.34 ± 0.22	1.23 ± 0.13
15100	342.173767	-44.545620	9.24 ± 0.12	-16.67 ± 0.05	5.48 ± 0.80
62329	342.164032	-44.525223	9.26 ± 0.52	-16.51 ± 0.18	3.04 ± 0.44
1567	342.246490	-44.569771	9.29 ± 3.67	-16.61 ± 1.28	1.22 ± 0.13
10727	342.272583	-44.551075	9.31 ± 0.23	-18.00 ± 0.07	1.23 ± 0.13
2360	342.242371	-44.567291	9.33 ± 1.07	-16.67 ± 0.35	1.24 ± 0.14
41930	342.233246	-44.538322	9.33 ± 0.37	-17.10 ± 0.12	1.56 ± 0.19
1797	342.256927	-44.568947	9.35 ± 0.61	-16.40 ± 0.20	1.21 ± 0.13
1675	342.252380	-44.569401	9.37 ± 0.74	-16.52 ± 0.24	1.21 ± 0.13
73377	342.242371	-44.567303	9.39 ± 3.85	-16.72 ± 1.34	1.24 ± 0.14
11464	342.234955	-44.549992	9.41 ± 0.65	-17.74 ± 0.21	1.38 ± 0.17
57073	342.161499	-44.521320	9.41 ± 0.27	-16.79 ± 0.09	2.21 ± 0.30
70473	342.198578	-44.535030	9.41 ± 0.41	-15.92 ± 0.14	4.42 ± 0.74
3268	342.242767	-44.564835	9.43 ± 4.18	-17.20 ± 1.46	1.25 ± 0.14
47627	342.235321	-44.542278	9.43 ± 0.44	-16.63 ± 0.14	1.46 ± 0.17
5710	342.214111	-44.559807	9.44 ± 0.28	-17.35 ± 0.09	1.43 ± 0.17
63930	342.161499	-44.525753	9.52 ± 0.03	-18.27 ± 0.01	2.82 ± 0.43
13276	342.181305	-44.547470	9.56 ± 0.51	-15.55 ± 0.17	3.00 ± 0.41
55592	342.182129	-44.520252	9.67 ± 0.42	-16.36 ± 0.15	7.14 ± 1.28
48785	342.160278	-44.541546	9.88 ± 0.38	-15.26 ± 0.13	7.72 ± 1.52
1791	342.236115	-44.568989	9.89 ± 0.38	-17.14 ± 0.12	1.25 ± 0.14
4357	342.231903	-44.562424	9.92 ± 0.50	-16.50 ± 0.15	1.30 ± 0.15
48074	342.195038	-44.542713	9.99 ± 3.95	-15.56 ± 1.34	2.63 ± 0.36
10544	342.257294	-44.551338	10.07 ± 4.35	-16.65 ± 1.41	1.27 ± 0.14
22732	342.234650	-44.530128	10.10 ± 0.53	-17.00 ± 0.16	1.68 ± 0.21
53230	342.199005	-44.518162	10.12 ± 0.54	-13.15 ± 0.29	41.40 ± 9.85

Table A2. Continued the Table A1.

ID	RA(J2000)	DEC(J2000)	z_{phot}	$M_{\text{UV}}[\text{mag}]$	μ
2280	342.230560	-44.567539	10.15 ± 0.27	-17.85 ± 0.08	1.28 ± 0.15
23154	342.234375	-44.530270	10.15 ± 0.45	-17.35 ± 0.14	1.68 ± 0.21
54189	342.198242	-44.519115	10.16 ± 0.56	-12.89 ± 2.93	81.56 ± 138.65
2470	342.237244	-44.566978	10.20 ± 0.33	-17.50 ± 0.10	1.26 ± 0.14
40398	342.155487	-44.537029	10.21 ± 0.58	-16.59 ± 0.18	4.12 ± 0.59
983	342.250427	-44.571609	10.25 ± 0.66	-17.04 ± 0.19	1.21 ± 0.13
55874	342.190979	-44.542007	10.46 ± 4.01	-15.72 ± 1.31	3.55 ± 0.53
73273	342.236664	-44.564953	10.56 ± 0.61	-16.61 ± 0.17	1.27 ± 0.14
18900	342.162781	-44.528698	10.57 ± 0.63	-15.42 ± 0.19	3.96 ± 0.62
9638	342.257690	-44.552753	10.61 ± 0.72	-16.89 ± 0.20	1.26 ± 0.14
11545	342.221802	-44.549793	10.61 ± 0.50	-16.75 ± 0.14	1.48 ± 0.17
55303	342.185425	-44.520073	10.70 ± 4.21	-15.12 ± 1.47	14.82 ± 3.05
70775	342.198120	-44.536846	10.70 ± 3.44	-15.23 ± 1.08	3.77 ± 0.59
4305	342.217743	-44.562569	10.82 ± 0.60	-16.66 ± 0.17	1.41 ± 0.16
41490	342.250214	-44.538063	10.82 ± 4.06	-17.43 ± 1.19	1.39 ± 0.16
46385	342.198792	-44.541153	10.89 ± 0.67	-15.97 ± 0.19	2.62 ± 0.36
51235	342.190857	-44.515186	10.91 ± 0.74	-15.52 ± 0.22	4.10 ± 0.61
13413	342.178345	-44.547295	10.96 ± 0.35	-16.11 ± 0.10	3.60 ± 0.47
13593	342.182129	-44.547195	10.99 ± 0.27	-17.02 ± 0.08	3.04 ± 0.41
10172	342.244080	-44.551899	11.00 ± 1.48	-17.01 ± 0.40	1.38 ± 0.16
69853	342.208374	-44.530537	11.14 ± 0.82	-15.82 ± 0.23	3.41 ± 0.53
5517	342.237762	-44.5601200	11.30 ± 0.27	-17.60 ± 0.07	1.29 ± 0.14
56130	342.194855	-44.542469	11.32 ± 4.85	-15.09 ± 1.45	2.69 ± 0.38
72189	342.252869	-44.545906	11.39 ± 0.43	-16.90 ± 0.11	1.32 ± 0.15
6874	342.223267	-44.557743	11.55 ± 0.21	-16.98 ± 0.05	1.38 ± 0.16
44018	342.204620	-44.539558	11.63 ± 4.27	-18.21 ± 1.14	1.26 ± 0.14
68320	342.177917	-44.518085	11.74 ± 0.58	-16.69 ± 0.15	3.26 ± 0.52
6880	342.223328	-44.557713	11.76 ± 0.23	-16.67 ± 0.06	1.38 ± 0.16
11945	342.263031	-44.549343	11.77 ± 4.29	-17.97 ± 1.13	1.26 ± 0.14
1781	342.239868	-44.569035	11.85 ± 0.18	-16.92 ± 0.04	1.25 ± 0.14
4213	342.264160	-44.562721	11.90 ± 0.81	-17.26 ± 0.20	1.21 ± 0.14
12189	342.265320	-44.548908	11.99 ± 0.31	-17.61 ± 0.08	1.29 ± 0.14
10313	342.192139	-44.551685	13.78 ± 5.40	-16.79 ± 1.21	1.38 ± 0.16
57696	342.168823	-44.521694	14.15 ± 1.77	-15.32 ± 0.40	5.42 ± 0.90
71717	342.248749	-44.542152	14.81 ± 1.26	-17.36 ± 0.24	1.36 ± 0.16